Decaying turbulence in an active-grid-generated flow and comparisons with large-eddy simulation

By HYUNG SUK KANG[1], STUART CHESTER[1]
AND CHARLES MENEVEAU[1,2]

[1]Department of Mechanical Engineering, The Johns Hopkins University, 3400 North Charles Street,
Baltimore, MD 21218, USA

[2]Center for Environmental and Applied Fluid Mechanics, The Johns Hopkins University,
3400 North Charles Street, Baltimore, MD 21218, USA

Measurements of nearly isotropic turbulence downstream of an active grid are performed as a high-Reynolds-number ($Re_\lambda \approx 720$) update of the Comte-Bellot & Corrsin (1971) data set. Energy spectra at four downstream distances from the grid, ranging from $x/M = 20$ to $x/M = 48$, are measured and documented for subsequent initialization of, and comparison with, large-eddy simulations (LES). Data are recorded using an array of four X-wire probes which enables measurement of filtered velocities, filtered in the streamwise (using Taylor's hypothesis) and cross-stream directions. Different filter sizes are considered by varying the separation between the four probes. Higher-order statistics of filtered velocity are quantified by measuring probability density functions, and hyper-flatness and skewness coefficients of two-point velocity increments. The data can be used to study the ability of LES to reproduce both spectral and higher-order statistics of the resolved velocity field. In this study, the Smagorinsky, dynamic Smagorinsky, and dynamic mixed nonlinear models are considered. They are implemented in simulations of decaying isotropic turbulence using a pseudospectral code with initial conditions that match the measured energy spectra at $x/M = 20$. Overall, it is found that the various LES models predict accurate low-order statistics of resolved scales in isotropic turbulence during the decay. For the spectral cutoff filter, the dynamic Smagorinsky model simulates the energy spectrum more closely at smaller wavenumber, and the dynamic mixed nonlinear model has closer agreement at large wavenumber. For the graded physical-space (Gaussian) filter, the dynamic mixed nonlinear model provides the best spectral results. The three models considered here underpredict the intermittency of longitudinal velocity increments at small distances. For transverse velocity increments, the models' predictions are closer to the measured values, but differ among themselves, with the mixed nonlinear model predicting reduced intermittency. Comparisons of probability density functions of subgrid-scale dissipation and stresses from simulations and experimental data reveal pronounced differences among the different models.

1. Introduction

Decaying isotropic turbulent flow has long served as important benchmark test case for turbulence theories, models, and computer simulations. Probably the best-known data of decaying isotropic turbulence are provided by the grid experiments of Comte-Bellot & Corrsin (1971). This classic data set includes turbulence kinetic energy,

decay rate, correlation functions, and one- and three-dimensional energy spectra. Owing to the availability of three-dimensional energy spectra at various times during the decay which allow initialization of numerical simulations and spatial filtering, the Comte-Bellot & Corrsin (1971) data have been particularly useful in the context of large-eddy simulations (LES). In LES, the turbulent fields are decomposed into their small- (subgrid-) scale and large- (resolved-) scale components by spatial filtering with a kernel, $G_\Delta(x)$, of characteristic size Δ (see Leonard 1974, and reviews by Lesieur & Métais 1996; Piomelli 1999; and Meneveau & Katz 2000). By applying the filtering operation to the Navier–Stokes equations, the LES equations for the filtered velocity field $\widetilde{u}(x, t)$ are obtained. These equations are unclosed because they contain the so-called subgrid-scale (SGS) stress tensor that accounts for momentum transport caused by unresolved motions. To close the LES equations, the SGS stress tensor is expressed as a function of the resolved velocity field.

The success of various SGS models is often gauged by the ability of simulations to reproduce the statistics of resolved motion, and decaying isotropic turbulence is one of the simplest test cases. LES studies that have utilized the Comte-Bellot & Corrsin (1971, denoted henceforth as CBC) data include, among others, Moin *et al.* (1991); Dantinne *et al.* 1998; Meneveau, Lund & Cabot (1996); Misra & Pullin (1997); and Ackermann & Métais (2001). In these studies, simulations are initialized using the radial three-dimensional spectrum deduced (assuming isotropy) from the longitudinal one-dimensional spectrum at the initial distance downstream of the grid (in CBC at $x/M = 42$, where x is the downstream distance and $M = 5.08$ cm is the mesh size of the grid). Energy spectra measured at two further downstream stations (at $x/M = 98$ and $x/M = 171$) can be compared with the temporal evolution of the simulated velocity fields' energy spectra. Since in LES the simulated fields correspond to spatially filtered turbulence ($\widetilde{u}(x, t)$), the measured spectra are multiplied by the filter transfer function, $|\widehat{G}_\Delta(\kappa)|^2$. In this fashion, the CBC data have been used in detailed comparisons with simulations, based on the two-point statistics and energetics of the flow, filtered at scales of interest in the context of LES. Comparisons with simulations have shown, for instance, that the standard and dynamic Smagorinsky models lead to a small 'pile-up' of energy spectra near the cutoff wavenumber (Moin *et al.* 1991 and Meneveau *et al.* 1996), an issue that has motivated various spectral and hyper eddy viscosity models (see e.g. Lesieur & Métais 1996 and Cerutti, Meneveau & Knio 2000).

Two important limitations of the CBC data for the purpose of testing LES are that only second-order statistics (spectra) are reported, and that the Reynolds number is low. More recent measurements in decaying grid turbulence reported in Cerutti & Meneveau (2000) have addressed the first limitation by using an array of X-wire probes which provided data that could be filtered spatially with a fixed filter size. In this fashion, time series of filtered velocity were used to document probability density functions (PDFs) and higher-order moments of filtered velocity. The Reynolds number of the grid turbulence experiments was larger than those in CBC (about $Re_\lambda \sim 150$), but that still can be considered moderate. Cerutti & Meneveau (2000) did not perform comparisons of the measured data with LES.

The main objectives of this study are to update the results of Comte-Bellot & Corrsin (1971) based on turbulence at high Reynolds number, and to provide more data and details of interest in studies of LES. Measurements are performed downstream of an 'active grid' that generates high-Reynolds-number turbulence in a range of Re_λ from about 720 to 630. In §2, the experimental apparatus and active grid are described. Characteristics of the flow are presented in §3. As in Cerutti & Meneveau (2000) data are acquired using an array of four X-wires so that statistics

of filtered velocity can be characterized. In the present probe array, the separation distance between probes can be varied, allowing us to implement several filter sizes during post-processing. Results from the experiments, including measured spectra and higher-order statistics of filtered turbulence are presented in §4. Finally, this paper also presents numerical simulations of decaying isotropic turbulence using several well-known subgrid models. Detailed comparisons between LES and the measurements are presented in §5, and conclusions are drawn in §6.

2. Experimental apparatus and active grid

Wind tunnels of normal laboratory size with a conventional passive grid allow us to generate only moderate-Reynolds-number turbulence, with Taylor microscale Reynolds numbers typically not exceeding 150. The main reason is that the root-mean-square (r.m.s.) velocity developing downstream of a passive grid is relatively low. As an alternative, several studies have focused on 'active grids'. One option was proposed by Gad-el-Hak & Corrsin (1974), in which grids with evenly distributed jets inject secondary fluid into the flow. This apparatus yielded a modest increase in Reynolds number (to about $Re_\lambda \sim 160$). Recently, Makita (1991) and Mydlarski & Warhaft (1996) have developed an active grid arrangement in which randomly rotating agitator winglets add turbulent kinetic energy to the flow. They have achieved $Re_\lambda \approx 400$–500 with a turbulence intensity range of 9.5%–20%. More recently, Mydlarski & Warhaft (1998) built a scaled-up active grid (the mesh spacing of 11.4 cm was 2.25 times larger than that in Mydlarski & Warhaft 1996) and a maximum Reynolds number of $Re_\lambda \approx 730$ with a turbulence intensity of 17.4% at $x/M = 31$ was achieved.

The isotropy ratio (ratio of streamwise to transverse r.m.s. velocities) in the present study was about 1.15 far behind the active grid. This value is larger than that of the conventional passive-grid-generated turbulence that displays isotropy ratios typically less than 1.1. The larger anisotropy is caused by the relative spatial orientation of the agitator winglets, in which all winglets on a shaft are fixed in the same plane ('in-plane orientation'). In an effort to decrease the anisotropy, Poorte (1998) has proposed a 'staggered orientation' in which two adjacent winglets on a shaft are fixed perpendicular to each other so that the obstructions in the streamwise and cross-stream directions are nearly the same. When the rotation velocity of the winglet, time interval and initial angle of the winglets are sufficiently randomized, isotropy ratios in a range between 0.95 and 1.1 can be obtained. However, the r.m.s. velocities are then significantly lower than with the 'in-plane orientation' (e.g. Poorte 1998 obtained a maximum Re_λ of about 200). Since the present study concerns the dynamics of high-Reynolds-number turbulence, we have built an active grid system following the 'in-plane orientation' approach of Mydlarski & Warhaft (1996, 1998). Deviations from isotropy will be shown to be restricted to the very lowest wavenumbers of the flow and of little concern for detailed comparisons with LES and models.

Experiments are performed downstream of an active grid in the return-type Corrsin wind tunnel (Comte-Bellot & Corrsin 1966, 1971). The wind tunnel has primary and secondary contraction ratios of 25:1 and 1.27:1, respectively. The active grid is placed downstream of the secondary contraction. While an upstream placement would have been desirable for decreasing the anisotropy (see CBC, and also the very recent large active grid experiments of Larssen & Devenport 2002), existing support structures prevent efficient placement of the active grid apparatus at that location. The test section length is 10 m and the cross-section is 1.22 m by 0.91 m. The spanwise width
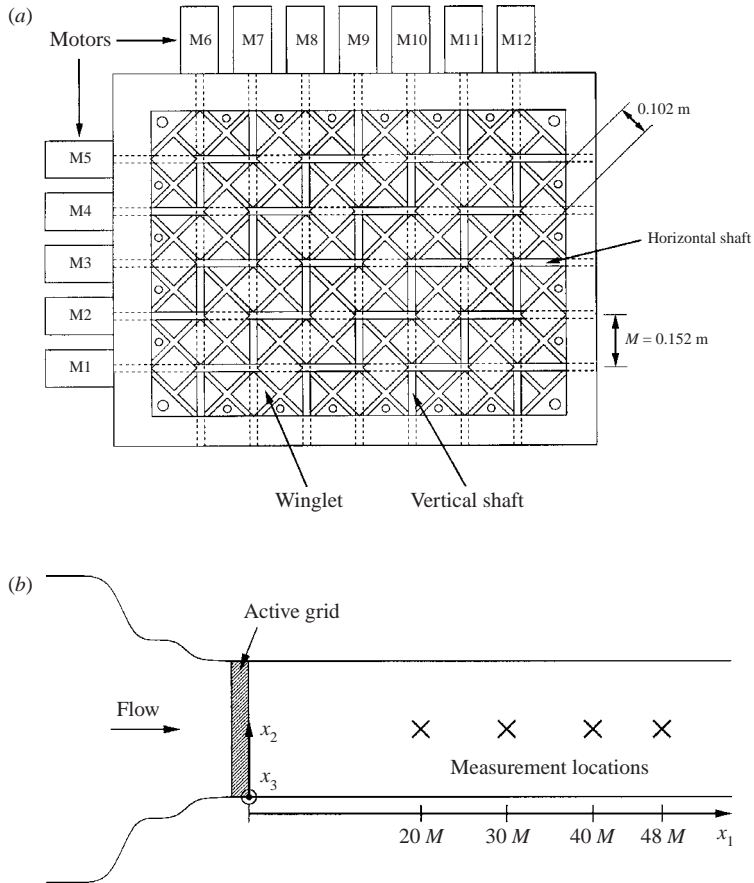
FIGURE 1. (*a*) Schematic of the active grid system; (*b*) schematic of the wind tunnel.

of the wind tunnel gradually increases along the test section to account for boundary layer growth.

The design of the active grid follows that of Makita (1991) and Mydlarski & Warhaft (1996, 1998). The active grid is composed of five horizontal and seven vertical rotating shafts to which diamond-shaped winglets are attached. The shafts are made of 19.05 mm square aluminium channel with 3.18 mm-thick walls. The horizontal and vertical shafts have eight and six winglets, respectively, so that the grid size, M, is 0.152 m. The $0.102 \times 0.102 \, \text{m}^2$ square winglets are made of 3.18 mm-thick aluminium plate. Along each shaft, the winglets are attached to opposite sides in an alternating fashion to help reduce vibrations. A schematic of the active grid is shown in figure 1(*a*). Each shaft is independently driven by a 1/4 hp AC motor (Baldor Industrial Motor, CNM20252) and each motor is controlled by an inverter (ABB Industrial Systems Inc., ACS 140). The control signal is generated by a PC and sent to the twelve inverters through two six-node RS-485 serial networks, using a National Instruments AT-485 card. Each motor is set to randomly change rotational speed and direction once every second. The speed is selected from a uniform distribution in the range of about 210–420 r.p.m., in both directions.

A schematic of the experimental wind-tunnel setup is shown in figure 1(*b*). The active grid is located at the beginning of the test section. The measurement locations

in the streamwise (longitudinal) direction (x_1) are at $x_1/M = 20$, 30, 40 and 48. To obtain the filtered velocities, an X-wire probe array described in Kang & Meneveau (2001) is used for measuring two velocity components in the (x_1, x_2)-plane. The velocity components in the (x_1, x_3)-plane can also be measured by rotating the probe by $90°$ in roll angle. Here x_2 and x_3 are the cross-stream (transverse, i.e. vertical and perpendicular to x_1) and spanwise (i.e. horizontal and perpendicular to x_1) directions, respectively. The probe array is composed of four custom-made miniature X-type hot-wire probes. Each probe holder was designed to slide smoothly in the cross-stream direction on two supporting rods, so the separation distance, s, between the probes in the cross-stream direction x_2 could be adjusted manually between 5 and 60 mm. As in Cerutti & Meneveau (2000) and Kang & Meneveau (2001), we use a filter scale equal to twice the distance between two probes (i.e. $\Delta = 2s$) during data analysis. Four different filter scales of $\Delta_1 = 10$ mm, $\Delta_2 = 20$ mm, $\Delta_3 = 40$ mm, and $\Delta_4 = 80$ mm are considered. An intermediate configuration with $s = 20$ mm (and $\Delta_3 = 40$ mm) is selected as a reference filter scale in the present study.

Each probe contains two 2.5 μm platinum-coated tungsten wires which are copper-plated and soldered to the X-wire prong ends and etched, yielding an active length-to-diameter ratio of about 200. The wire spacing between the hot wires is 0.5 mm. The eight hot wires are operated in constant-temperature anemometry (CTA) mode by TSI IFA300 units. The overheat ratio of the hot wires is about 1.6. The signals are sampled at $f_s = 40$ kHz, low-pass filtered at a frequency of 20 kHz and digitized with a 12-bit simultaneous sample and hold A/D converter (United Electronic Industries, WIN-30DS). The sampling time is 30×30 s, so the total number of data points per channel for each measurement location is 36×10^6. The array is located at the centre of the wind tunnel and is moved manually to various downstream locations.

All four X-wire probes with a separation distance of $s = 5$ mm are calibrated simultaneously in the core region of an axisymmetric calibration jet. As a result, the differences of the mean and r.m.s. velocities from different probes are small, within 2.0%. The velocity calibration of the X-wire probes is performed at a fixed temperature at 15 different jet-exit velocities ranging from 3 m s^{-1} to 18 m s^{-1} and for nine different yaw angles under a constant jet velocity of 11.4 m s^{-1}. To account for temperature increase during the experiment, the velocity calibration of the hot wires is repeated at the four different fixed temperatures of 18.3 °C, 24.3 °C, 26.7 °C and 31.2 °C, covering the temperature variations during the measurements. The temperature is measured by an Omega DP25 with a J-type sub-miniature thermocouple (JMQSS-010E-6). We use fourth-order polynomials as a function of output voltage depending on temperature as the calibration curves. The full calibration procedure is performed before and after the 13-hour measurements from $x_1/M = 20$ to $x_1/M = 48$. All the hot-wire anemometers give stable signals. Velocity differences from the two calibration sets are below 2%. At each measurement location (fixed x_1/M), the data for different filter scales are sampled sequentially. Data for all four filter scales are acquired at $x_1/M = 20$ and 48, while only one filter scale ($\Delta_1 = 10$ mm) is considered at $x_1/M = 30$ and 40.

3. Flow characteristics

The inhomogeneities in streamwise mean velocity $\langle u_1 \rangle$, and r.m.s. velocities $u_{1\text{r.m.s.}}$ and $u_{2\text{r.m.s.}}$ in the central core region (0.25 m $< x_2 < 0.65$ m and 0.25 m $< x_3 < 0.95$ m)

	$x_1/M = 20$	$x_1/M = 30$	$x_1/M = 40$	$x_1/M = 48$
$\langle u_1 \rangle$ (m s^{-1})	12.0	11.2	11.0	10.8
$u_{1\text{r.m.s.}}$ (m s^{-1})	1.85	1.43	1.19	1.08
$u_{2\text{r.m.s.}}$ (m s^{-1})	1.64	1.25	1.04	0.932
$I = u_{1\text{r.m.s.}}/u_{2\text{r.m.s.}}$	1.13	1.14	1.14	1.16
$u_{1\text{r.m.s.}}/\langle u_1 \rangle$ (%)	15.4	12.8	10.8	10.0
ϵ (m^2 s^{-3})	22.8	9.13	4.72	3.41
ϵ^{decay} (m^2 s^{-3})	24.5	9.85	5.15	3.42
$\ell = 0.9u_{1\text{r.m.s.}}^3/\epsilon$ (m)	0.250	0.288	0.321	0.332
η (mm)	0.11	0.14	0.16	0.18
λ (mm)	5.84	7.13	8.25	8.78
$Re_M = \langle u_1 \rangle M/\nu$	1.21×10^5	1.13×10^5	1.11×10^5	1.09×10^5
$Re_\lambda = u_{1\text{r.m.s.}}\lambda/\nu$	716	676	650	626
$Re_\ell = u_{1\text{r.m.s.}}\ell/\nu$	30,600	27,300	25,300	23,700

TABLE 1. Parameters of active-grid-generated flow. For all cases, the number of data points per channel is 36×10^6. Deviations from one probe to another are typically of 2% for mean velocity, 2% for r.m.s. values, and 6% for dissipation.

at $x_1/M = 20$ are 5.1%, 3.8%, and 4.1%, respectively (largest deviation from centreline values). The spanwise r.m.s. velocities $u_{3\text{r.m.s.}}$ at the measurement locations at the centreline of the wind tunnel agree with $u_{2\text{r.m.s.}}$ to within 1.5%, and the energy spectra $E_{22}(\kappa_1)$ and $E_{33}(\kappa_1)$ coincide well with each other.

Table 1 shows the main parameters of each experimental data set, including the streamwise mean velocity $\langle u_1 \rangle$, the r.m.s. velocities $u_{1\text{r.m.s.}}$ and $u_{2\text{r.m.s.}}$, the isotropy ratio $I = u_{1\text{r.m.s.}}/u_{2\text{r.m.s.}}$, the turbulence intensity $u_{1\text{r.m.s.}}/\langle u_1 \rangle$, the molecular kinetic energy dissipation rate ϵ (its determination is described below), the integral scale defined as $\ell = 0.9u_{1\text{r.m.s.}}^3/\epsilon$ (Mydlarski & Warhaft 1998), the Kolmogorov length scale $\eta = (\nu^3/\epsilon)^{1/4}$, the Taylor microscale λ, and Reynolds numbers. Deviations from one probe to another are typically 2% for mean velocity, 2% for r.m.s. values, and 6% for dissipation derived as described below. To obtain the spatial quantities in the streamwise direction from the temporal data, Taylor's hypothesis is invoked.

Since the diameter of the measurement volume ($\approx 0.5\,\text{mm}$) of the X-wire probe is about five times larger than the Kolmogorov length scale η, the dissipation scale is not sufficiently resolved in the present experiments. Therefore, the molecular kinetic energy dissipation rate ϵ cannot be obtained accurately from the derivative variance and is obtained instead from the third-order structure function as described in Lindborg (1999) and Cerutti & Meneveau (2000). Specifically, we correct for the finite Reynolds number and inhomogeneity effects by applying the procedure suggested by Lindborg (1999). The approach is based on the full Kolmogorov equation for locally isotropic turbulent flow (Lindborg 1999), as

$$D_{uuu}(r,t) \equiv \langle [u_1(x_1 + r, t) - u_1(x_1, t)]^3 \rangle = -\tfrac{4}{5}\epsilon r + 6\nu \frac{\partial D_{uu}}{\partial r} - \frac{3}{r^4} \int_0^r r'^4 \frac{\partial D_{uu}}{\partial t}\, \text{d}r', \quad (1)$$

where D_{uu} is the second-order structure function, i.e. $D_{uu}(r,t) \equiv \langle [u_1(x_1 + r, t) - u_1(x_1, t)]^2 \rangle$. The second term on the far right-hand side of equation (1) shows the effect of the diffusivity, and becomes negligible at sufficiently large Reynolds numbers for r in the inertial range ($r \gg \eta$). The last term represents the decay in the mean flow direction.
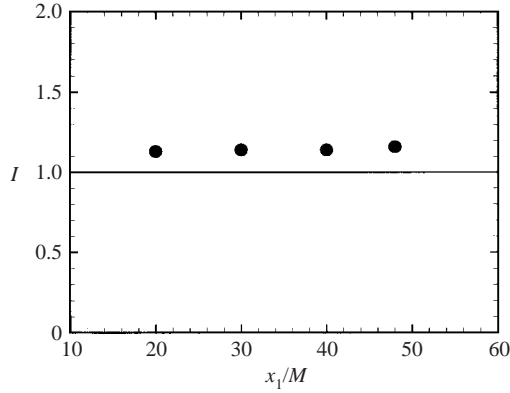
FIGURE 2. Isotropy ratios, $I = u_{1\text{r.m.s.}}/u_{2\text{r.m.s.}}$, in the downstream direction in an active-grid-generated decaying turbulence.

To calculate $\partial D_{uu}/\partial t$ in equation (1), Kolmogorov's second similarity hypothesis ($D_{uu} = C\epsilon^{2/3}\,r^{2/3}$) and the k–ϵ model for the decay of the molecular dissipation ($\partial\epsilon/\partial t = -C_{\epsilon 2}\,\epsilon^2/k$) are used. We choose $C = 2.0$ (this value falls in the range $1.9 \leqslant C \leqslant 2.3$ as suggested by Sreenivasan 1995), and the standard value $C_{\epsilon 2} = 1.92$ is used. Also, $k \equiv \frac{3}{2}u_{1\text{r.m.s.}}^2$ is the turbulent kinetic energy. Then, equation (1) becomes

$$\frac{D_{uuu}}{\epsilon r} = -\frac{4}{5} + C\left[4\left(\frac{r}{\eta}\right)^{-4/3} + \frac{4\sqrt{15}C_{\epsilon 2}}{17}\frac{\nu}{u_{1\text{r.m.s.}}\lambda}\left(\frac{r}{\eta}\right)^{2/3}\right]. \tag{2}$$

This is equivalent to equation (6) in Lindborg (1999). The molecular kinetic energy dissipation rate in equation (2) is determined by iteration starting from its initial guess (the peak value of $-\frac{5}{4}D_{uuu}(r)/r$ in the inertial range). Calculated in this fashion, ϵ is 20%–23% higher than the peak value of $-\frac{5}{4}D_{uuu}(r)/r$. These differences are comparable to those obtained in Cerutti & Meneveau (2000), and are also similar to the trends of a recent analysis of the two-thirds law based on matched asymptotic expansions in Lundgren (2002). The modification of C to 2.1 results in only a 1% increase in ϵ, and a $\pm 10\%$ change of $C_{\epsilon 2}$ makes only a $\pm 2.4\%$ change in ϵ (e.g. using $C_{\epsilon 2} = (n + 1)/n = 1.8$ from the measured value of $n = 1.25$ – see §4.1 below – would give only a -1% change in ϵ).

When the molecular kinetic energy dissipation rates are measured directly from the decay of the turbulent kinetic energy $\epsilon^{\text{decay}} = -\mathrm{d}k/\mathrm{d}t$, the difference between ϵ and ϵ^{decay} is between 1% and 9%. Detailed determination of ϵ^{decay} is described in §4.1.

The Taylor scale is evaluated according to

$$\lambda = \left(15\frac{u_{1\text{r.m.s.}}^2\nu}{\epsilon}\right)^{1/2}. \tag{3}$$

The Taylor-scale Reynolds number is $Re_\lambda = u_{1\text{r.m.s.}}\lambda/\nu$. The isotropy ratio, I, is shown in figure 2. The present active-grid turbulence deviates from isotropy by about 15% over the measurement locations from $x_1/M = 20$ to 48. As already summarized in §1, similar or higher anisotropy is observed in other active-grid turbulence experiments with 'in-plane' winglet arrangements. Makita (1991) and Mydlarski & Warhaft (1996) reported $I = 1.22$ at $x_1/M = 50$ and $I = 1.21$ at $x_1/M = 68$, respectively. We have
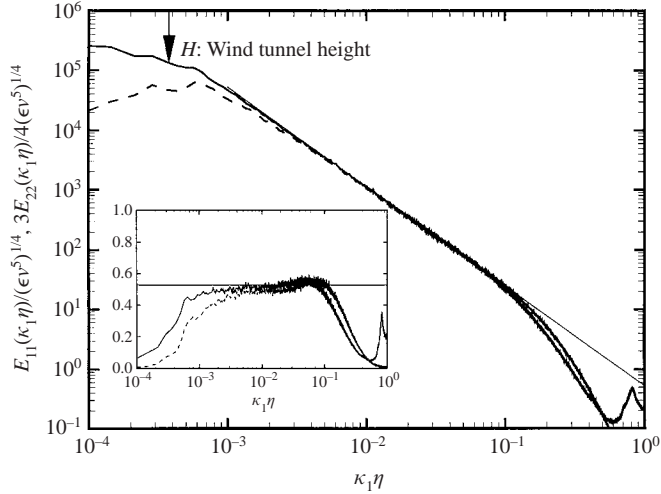
FIGURE 3. Longitudinal one-dimensional energy spectra in Kolmogorov units at $x_1/M = 20$. The solid and dashed lines represent the longitudinal spectrum of the u_1-component and the u_2-component multiplied by 3/4, respectively, as a function of the longitudinal wavenumber, κ_1. The inset shows the compensated spectra, $E_{11}(\kappa_1) \, \epsilon^{-2/3} \kappa_1^{5/3}$ and $\frac{3}{4} E_{22}(\kappa_1) \, \epsilon^{-2/3} \kappa_1^{5/3}$. The spectrum of the u_2-component is below that of u_1 at low wavenumber ($\kappa_1 \eta < 0.003$), and higher at high wavenumber ($0.1 < \kappa_1 \eta < 0.5$). The straight solid lines are the universal spectra with $-5/3$ power-law and a fitted $18/55c_K = 0.527$ intercept. The arrow corresponds to the wind tunnel height wavenumber, $\kappa_H = \pi/H$, with $H = 6M$.

also tested the 'staggered' (alternating) winglet orientation. The measured isotropy ratio was reduced to 1.10, but also the Taylor-scale Reynolds number decreased to $Re_\lambda = 350$ at $x_1 = 20M$. To maintain high-Reynolds-number conditions, we select the 'in-plane orientation', and document the remaining anisotropy using energy spectra.

Figure 3 shows energy spectra of unfiltered turbulence at $x_1/M = 20$. Both the longitudinal spectrum $E_{11}(\kappa_1)$ of the u_1-component (solid line) and the longitudinal spectrum $E_{22}(\kappa_1)$ of the u_2-component, multiplied by 3/4 (dashed line) are presented. Here, κ_1 is the longitudinal wavenumber. Statistically very well-converged spectra are calculated by partitioning the data set into 2100 segments (with 50% overlapping) of 2^{15} points each. The segments are windowed with a Barlett window. Since the noise peak in the longitudinal spectrum of u_1 is in the far dissipation region, quite removed from any of the filter frequencies and scales of interest in this study, no effort is made to remove the noise by additional filtering.

As seen in the compensated spectrum shown in the inset, the Kolmogorov constant c_K in $E_{11}(\kappa_1) = \frac{18}{55} c_K \epsilon^{2/3} \kappa_1^{-5/3}$ is obtained as $c_K \approx \frac{55}{18}(0.527) \approx 1.61$, consistent with the standard value of about 1.6 (Sreenivasan 1995). It can be clearly observed that $E_{11}(\kappa_1) \approx \frac{3}{4} E_{22}(\kappa_1)$ as required by isotropy in the inertial range, over at least one and a half decades of wavenumber. Differences between the spectra at the large scales (low wavenumbers) occur at the end of the power-law region near wavenumbers corresponding to the wind tunnel height ($\kappa_H = \pi/H$, where $H = 6M$ is the wind-tunnel height). Therefore, we conclude that the anisotropy shown in figure 2 is due to large-scale motion of size comparable to the wind tunnel height, while inertial-range dynamics follow isotropic behaviour.
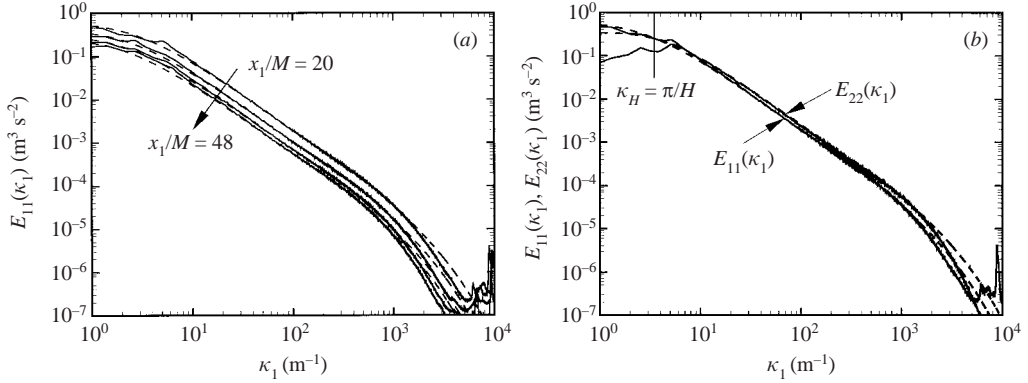
FIGURE 4. Measured longitudinal spectra (solid lines). (a) E_{11} at $x_1/M = 20, 30, 40$ and 48. (b) E_{11} and E_{22} at $x_1/M = 20$. The dashed lines are fitted spectra from equations (4) and (5).

4. Results

4.1. *Evolution of energy spectra*

Longitudinal spectra of streamwise velocity at the various downstream distances are shown in figure 4(a) (solid lines). For completeness, the corresponding data are reproduced in tabular form in the Appendix.

As in CBC, we wish to deduce from these data the corresponding radial three-dimensional energy spectrum $E(\kappa)$ by assuming small-scale isotropy. The one-dimensional and three-dimensional spectra (Batchelor 1953; Pope 2000) are related by

$$E_{11}(\kappa_1) = \int_1^\infty \frac{x^2 - 1}{x^3} E(\kappa_1 x) \, dx, \tag{4}$$

and

$$E_{22}(\kappa_1) = \frac{1}{2} \int_1^\infty \frac{x^2 + 1}{x^3} E(\kappa_1 x) \, dx, \tag{5}$$

where $x = \kappa/\kappa_1$.

The inverse relationship expressing the radial spectrum in terms of the measured longitudinal spectra involves differentiation (Batchelor 1953; Pope 2000). In order to avoid taking derivatives of measured spectra, and to include proper limiting conditions, a trial-and-error method already used in Cerutti & Meneveau (2000) is applied. The following functional form for the three-dimensional energy spectrum is assumed (Pope 2000; Cerutti & Meneveau 2000):

$$E(\kappa) = c_K \epsilon^{2/3} \kappa^{-5/3} \left[\frac{\kappa\ell}{[(\kappa\ell)^{\alpha_2} + \alpha_1]^{1/\alpha_2}} \right]^{5/3 + \alpha_3} e^{-\alpha_4 \kappa \eta}$$

$$\times \left[1 + \alpha_5 \left(\frac{1}{\pi} \arctan\{\alpha_6 \log_{10}(\kappa\eta) + \alpha_7\} + \tfrac{1}{2} \right) \right], \quad (6)$$

where c_K and α_i ($i = 1$ to 7) are parameters to be decided by comparing with measured data, and ℓ and ϵ are the integral length scale and dissipation at each measurement location as reported in table 1. In equation (6), $\kappa^{-5/3}$ represents the main scaling in the inertial range, and $(\kappa\ell/[(\kappa\ell)^{\alpha_2} + \alpha_1]^{1/\alpha_2})^{5/3 + \alpha_3}$, modified slightly from Pope (2000), reproduces the energy spectrum at low wavenumbers of $\kappa < 10 \, \text{m}^{-1}$. The $e^{-\alpha_4 \kappa \eta}$ factor
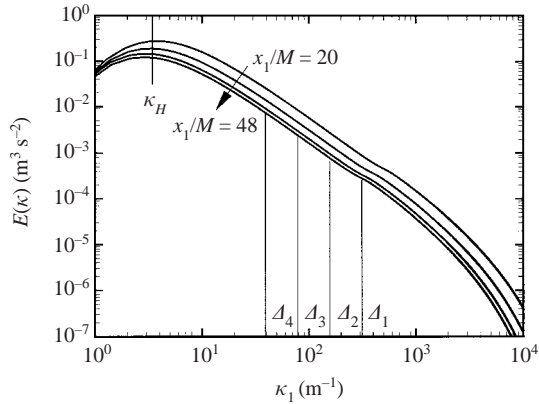
FIGURE 5. The three-dimensional energy spectra in the active-grid-generated decaying turbulence at $x_1/M = 20$, 30, 40 and 48 based on equation (6) with fitted parameters. The five vertical lines correspond to the wind tunnel height and four different filter scales of $\Delta_1 = 0.01$ m, $\Delta_2 = 0.02$ m, $\Delta_3 = 0.04$ m and $\Delta_4 = 0.08$ m. All the filter scales are in the inertial range.

represents the usual high-wavenumber decay in the dissipation region (owing to hot-wire attenuation we do not use the data to determine this decay but instead use the exponential decay recommended in Pope 2000). The arctangent factor goes from 1 at low wavenumbers to $1 + \alpha_5$ at high wavenumbers and reflects the bottleneck effect at $\kappa \sim 500$ m^{-1} which appears clearly in the spectra (attempts to fit without including the bottleneck term were noticeably less accurate). To find the parameters α_i the fitted one-dimensional energy spectra are calculated using equations (4) and (5) with $E(\kappa)$ written as in equation (6) with some assumed set of parameter values. Results are visually compared to the measured longitudinal spectra and the procedure is repeated until good agreement between the fitted and original one-dimensional spectra is achieved. The parameters finally selected are: $c_K = 1.613$, $\alpha_1 = 0.39$, $\alpha_2 = 1.2$, $\alpha_3 = 4.0$, $\alpha_4 = 2.1$, $\alpha_5 = 0.522$, $\alpha_6 = 10.0$, $\alpha_7 = 12.58$. These values produce good agreement with the measured longitudinal spectra for all four downstream locations, in the inertial range and the bottleneck wavenumber ranges. The comparison is shown for the streamwise velocity component in figure 4(*a*) (dashed lines). In the dissipation range, the fit decays less than the measured spectra at wavenumbers where one expects probe attenuation to occur. Figure 4(*b*) presents results for the transverse velocity component at $x_1/M = 20$, also showing good agreement and deviations from isotropy only near and below κ_H.

Finally, the three-dimensional radial energy spectra at all the measurement locations $x_1/M = 20$, 30, 40 and 48 based on the explicit smooth curve in equation (6) are shown in figure 5. Specifically, the energy spectrum at $x_1/M = 20$ can be used as initial energy distribution in LES of decaying isotropic turbulence. In figure 5 the five vertical lines correspond to the wind tunnel height and the four different filter scales of $\Delta_1 = 0.01$ m, $\Delta_2 = 0.02$ m, $\Delta_3 = 0.04$ m and $\Delta_4 = 0.08$ m. All the filter scales are in the inertial range.

In the present study, when reporting second-order statistics for filtered turbulence that can be derived from the spectral information (such as r.m.s. of filtered velocity) we will use the fitted spectra appropriately multiplied by the three-dimensional filter transfer function. For instance, the kinetic energy k of filtered turbulence (filtered
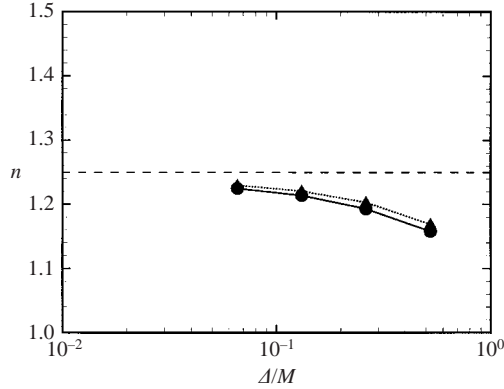
FIGURE 6. The decay exponent of the filtered kinetic energy as a function of the filter scale. The decay exponent of unfiltered kinetic energy obtained as the integral over the fitted three-dimensional spectrum is $n = 1.25$ (dashed line). Dotted line with triangles and solid line with circles represent decay exponents of kinetic energy for cutoff- and Gaussian-filtered velocities, respectively.

using a radial cutoff filter) is obtained by the integration of the three-dimensional radial energy spectrum according to

$$k \equiv \int_0^{\pi/\Delta} E(\kappa) \, d\kappa. \tag{7}$$

For a Gaussian-filtered field, the expression is

$$k \equiv \int_0^{\infty} E(\kappa) \, e^{-\Delta^2 \kappa^2/12} \, d\kappa. \tag{8}$$

The kinetic energy decay exponent n is traditionally defined as follows:

$$\frac{k}{\langle u_1 \rangle^2} \equiv A \left(\frac{x_1 - x_o}{M} \right)^{-n}, \tag{9}$$

where A is a fitting constant, and x_o the virtual origin. For the normalization parameter $\langle u_1 \rangle$ in equation (9), a fixed mean velocity of $11.2 \, \mathrm{m \, s^{-1}}$ (the average of all four downstream locations) is used. Good results are obtained with $x_o = 0$. Using a power-law fitting, the decay exponent of the unfiltered kinetic energy obtained from the integral over the fitted three-dimensional spectrum is $n = 1.25$. The same decay exponent was reported for both the rod grids and the disk grids by Comte-Bellot & Corrsin (1966). Figure 6 shows the decay exponents of filtered kinetic energy using both the spectral cutoff and Gaussian filters described above, as a function of filter scale. Both fall below the unfiltered kinetic energy decay exponent. The decay exponent of the filtered kinetic energy approaches 1.25 at small filter scales. At the largest filter scale, the decay rate is smaller, consistent with the idea that the larger eddies are associated with longer time scales. The decay exponent for a Gaussian-filtered field is slightly lower than for a cutoff-filtered field, since the Gaussian filter also damps out scales larger than the filter scale.

The evolution of the spectral-cutoff-filtered and Gaussian-filtered kinetic energy with various filter scales in the downstream direction are shown in figures 7(a) and 7(b), respectively. In both figures, the solid circles represent the unfiltered kinetic energy obtained as the integral over the fitted three-dimensional spectrum. As can be
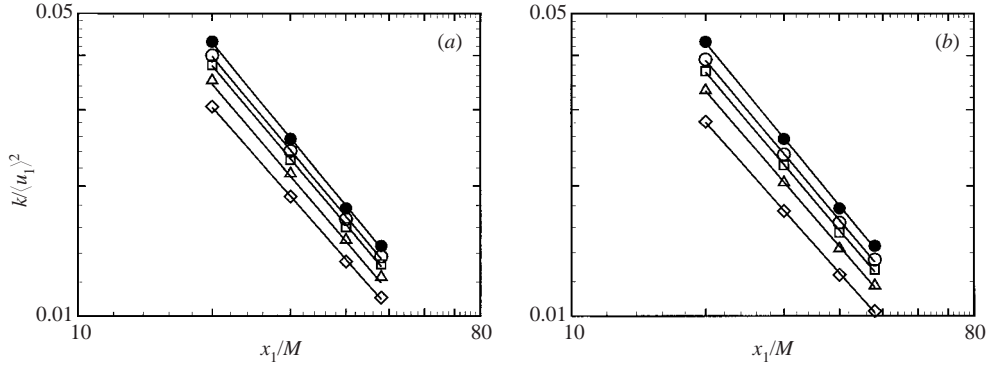
FIGURE 7. The evolution of the unfiltered and filtered kinetic energy with various filter scales in the downstream direction: (*a*) spectral cutoff filter; (*b*) Gaussian filter. Solid circles: the unfiltered kinetic energy obtained as the integral over the fitted three-dimensional spectrum. The open symbols represent the filtered kinetic energies at different filter scales: $\bigcirc$, $\Delta = \Delta_1$; $\square$, $\Delta = \Delta_2$; $\triangle$, $\Delta = \Delta_3$; $\diamond$, $\Delta = \Delta_4$. The solid lines represent the power-law fits using equation (9) with $x_o = 0$.

expected from figure 6, the filtered kinetic energy at a fixed x_1 and its slope decreases as the filter scale increases. The solid line represents the kinetic energy fitted by using the power-law fitting (equation (9)) with the decay exponents shown in figure 6. There is good agreement between the symbols and solid lines.

In addition to the value of ϵ obtained from D_{uuu}, the dissipation rate can now also be measured from the decay rate of kinetic energy as

$$\epsilon^{\text{decay}} = -\frac{\mathrm{d}k}{\mathrm{d}t} = -\langle u_1 \rangle \frac{\mathrm{d}k}{\mathrm{d}x_1} = nA \frac{\langle u_1 \rangle^3}{M} \left(\frac{x_1}{M} \right)^{-n-1}, \tag{10}$$

where $A = 1.80$ and $n = 1.25$. The values of ϵ^{decay} are 24.5, 9.85, 5.15, and 3.41 $\mathrm{m^2\,s^{-3}}$ at $x_1/M = 20$, 30, 40, and 48, respectively. These values differ by less than 9% from the dissipation rates shown in table 1 estimated by using the third-order structure function.

4.2. *Velocity-increment statistics at various scales*

In order to report more general statistics of filtered turbulence such as structure functions and PDFs that cannot be deduced from second-order statistics alone, the signals are first filtered using the full data from the probe array. There, to separate large and small scales, the two-dimensional box filter is applied to the streamwise and cross-stream directions, and the trapezoidal rule is used for the spatial integrations. As described in Cerutti & Meneveau (2000), the filtering process consists of a discrete approximation to a two-dimensional box filter. In the x_2-direction, a four-point discretization is used for evaluating the filtered velocity and SGS stresses. In the streamwise direction, the box filter is approximated using $f_s \Delta / \langle u_1 \rangle$ sampling points and the x_1-derivatives are evaluated using finite differences over a distance between the probes $s = \Delta/2$. A three-point approximation is used for the cross-stream derivatives of velocity that will be used later in §5.6. Filtered velocity gradients in the x_2-direction are evaluated using first-order finite differences over a distance s. The filtering and error analysis are documented in Cerutti & Meneveau (2000) and Cerutti *et al.* (2000).
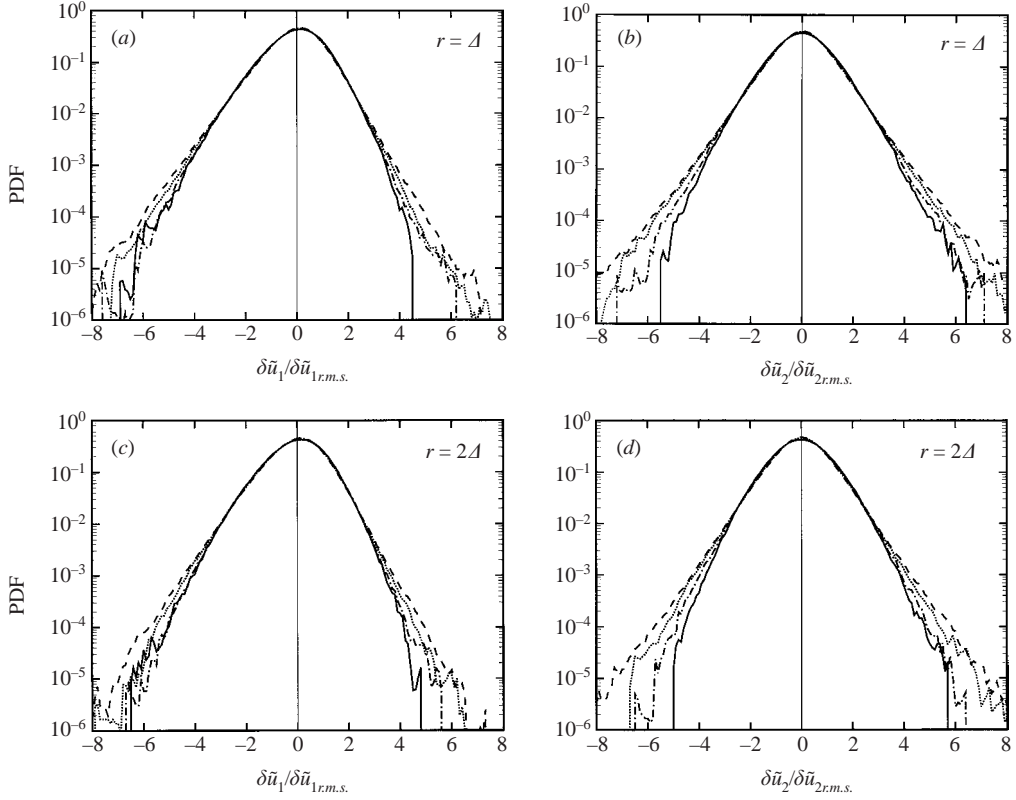
FIGURE 8. PDFs of filtered velocity increments measured at $x_1/M = 48$, for various filter sizes: Δ_1 (dashed line), Δ_2 (dotted line), Δ_3 (dash-dot line) and Δ_4 (solid line): (*a*) for streamwise velocity component at displacement $r = \Delta$, (*b*) for transverse velocity component at displacement $r = \Delta$, (*c*) for streamwise velocity component at displacement $r = 2\Delta$, (*d*) for transverse velocity component at displacement $r = 2\Delta$. Experimental data have been filtered using a graded filter in physical space.

The local structure of filtered velocity can be characterized by the increments defined as

$$\delta\widetilde{u}_i = \widetilde{u}_i(x_1 + r) - \widetilde{u}_i(x_1), \tag{11}$$

where r is the separation distance in the streamwise direction, and $i = 1$ (longitudinal velocity increment), or $i = 2$ (transverse velocity increment). We measure the filtered velocity-increment PDFs at two values of r and results are shown in figure 8. As expected, and consistent with prior results (Cerutti & Meneveau 2000), PDFs are more intermittent at smaller filter scales. These PDFs can be compared to simulation results to ascertain how well LES reproduces high-order statistics of resolved velocities. From the PDFs one can also deduce high-order moments of the filtered velocity increments at various displacement lengths (high-order structure functions). Also, in order to document the third-order statistics at more displacements, we measure the longitudinal structure-function skewness defined as

$$S \equiv \frac{\left\langle (\widetilde{u}_1(x_1 + r) - \widetilde{u}_1(x_1))^3 \right\rangle}{\left\langle (\widetilde{u}_1(x_1 + r) - \widetilde{u}_1(x_1))^2 \right\rangle^{3/2}}, \tag{12}$$
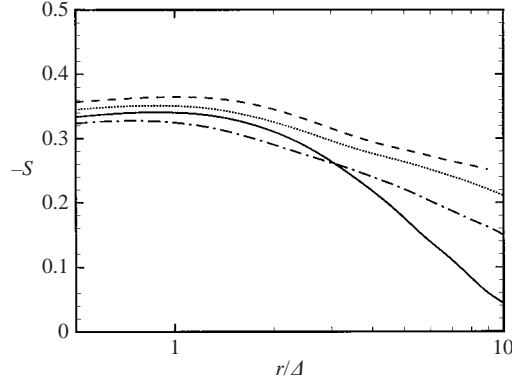
FIGURE 9. Skewness coefficient of filtered longitudinal velocity increments measured at $x_1/M = 48$ for various filter sizes: Δ_1 (dashed line), Δ_2 (dotted line), Δ_3 (dash-dot line) and Δ_4 (solid line).

where, again, r is the separation distance in the x_1-direction. S is typically negative due to the energy cascade across the resolved scales (Meneveau 1994). Results are shown in figure 9 as a function of displacement normalized by Δ for the four different filter scales considered. As can be seen in figure 9, the longitudinal structure-function skewness has a constant value of about -0.34 within 8% deviation at $r \sim \Delta$ for different filter scales. The magnitude of the skewness decreases as the separation distance increases, which is expected since the dynamics of velocity increments at scales larger than the inertial range become more Gaussian. At small values of r/Δ, the skewness of the velocity increments approaches the skewness of filtered velocity derivatives, which is known to be between -0.3 and -0.4 for Δ in the inertial range (Cerutti *et al.* 2000).

Having documented full second-order statistics and higher-order statistics of the filtered turbulence, in the next section we perform LES and compare details of simulation with experiment. In §5.6 some additional experimental data will be presented relating to SGS stress statistics and SGS dissipation.

5. Large-eddy simulation and *a posteriori* tests

The experimental data are used to compare with the statistics predicted from LES using several prototypical SGS models.

5.1. *Subgrid models*

As a simple case, we consider the classical Smagorinsky model (Smagorinsky 1963) which assumes quasi-equilibrium between large and small scales, and is as follows:

$$\tau_{ij}^{\text{Smag}} - \tfrac{1}{3}\tau_{kk}^{\text{Smag}}\delta_{ij} = -2\nu_T\widetilde{S}_{ij} = -2(C_S\Delta)^2|\widetilde{\mathbf{S}}|\widetilde{S}_{ij}, \tag{13}$$

where C_S is the Smagorinsky model coefficient, $\widetilde{S}_{ij} \equiv \tfrac{1}{2}(\partial\widetilde{u}_i/\partial x_j + \partial\widetilde{u}_j/\partial x_i)$ is the resolved strain-rate tensor and $|\widetilde{\mathbf{S}}| = (2\widetilde{S}_{mn}\widetilde{S}_{mn})^{1/2}$ is the modulus of the resolved strain-rate tensor. This model allows only forward energy transfer from the resolved scales to the subgrid scales, and is used in many applications.

Another model to be considered here is the 'nonlinear model' (Leonard 1974; Clark, Ferziger & Reynolds 1979; Liu, Meneveau & Katz 1994; Leonard 1997; Borue &

Orszag 1998; Meneveau & Katz 2000). The nonlinear model is as follows:

$$\tau_{ij}^{\mathrm{nl}} = C_{nl}\Delta^2 \widetilde{A}_{ki} \widetilde{A}_{kj}, \tag{14}$$

where $\widetilde{A}_{ki} \equiv \partial\widetilde{u}_i/\partial x_k$, C_{nl} is the nonlinear model coefficient and depends on the filter type and the test filter scale. This model has the realistic feature that it allows backscatter of energy, but requires the addition of an eddy viscosity part for various reasons, including numerical stability and better reproduction of geometric alignments of the SGS stress eigenvectors (Tao, Katz & Meneveau 2002). With this addition one obtains the mixed nonlinear model (see e.g. Anderson & Meneveau 1999):

$$\tau_{ij}^{\mathrm{mnl}} = -2(C_S\Delta)^2|\widetilde{\mathbf{S}}|\widetilde{S}_{ij} + C_{nl}\Delta^2 \widetilde{A}_{ki} \widetilde{A}_{kj}. \tag{15}$$

The model coefficients can be determined using the dynamic procedure proposed by Germano *et al.* (1991) from the resolved scales during the simulation. This procedure is based on the Germano identity (Germano *et al.* 1991),

$$L_{ij} \equiv T_{ij} - \overline{\tau}_{ij} = \overline{\widetilde{u}_i \widetilde{u}_j} - \overline{\widetilde{u}}_i \overline{\widetilde{u}}_j, \tag{16}$$

involving the difference between the SGS tensor at scale 2Δ, $T_{ij} = \overline{\widetilde{u}_i \widetilde{u}_j} - \overline{\widetilde{u}}_i \overline{\widetilde{u}}_j$, and the SGS tensor τ_{ij} test filtered at scale 2Δ. Note that an overline denotes test filtering at a scale 2Δ. Placing the Smagorinsky and mixed nonlinear models into (16), one obtains

$$L_{ij} - \tfrac{1}{3}L_{kk}\delta_{ij} = C_S^2 M_{ij}, \tag{17}$$

for the dynamic Smagorinsky model, and

$$L_{ij} = C_S^2 M_{ij} + C_{nl} N_{ij}, \tag{18}$$

where

$$M_{ij} \equiv -2\Delta^2 \left[4|\overline{\widetilde{\mathbf{S}}}|\overline{\widetilde{S}}_{ij} - \overline{|\widetilde{\mathbf{S}}|\widetilde{S}_{ij}} \right], \tag{19}$$

$$N_{ij} \equiv \Delta^2 \left[4\overline{\widetilde{A}}_{ki}\overline{\widetilde{A}}_{kj} - \overline{\widetilde{A}_{ki}\widetilde{A}_{kj}} \right], \tag{20}$$

for the dynamic mixed nonlinear model.

The average square errors from each model are given by

$$\mathscr{E}^{\mathrm{Smag}} = \langle L_{ij}^d L_{ij}^d \rangle - 2C_S^2 \langle L_{ij} M_{ij} \rangle + \left(C_S^2 \right)^2 \langle M_{ij} M_{ij} \rangle, \tag{21}$$

$$\mathscr{E}^{\mathrm{mnl}} = \langle L_{ij} L_{ij} \rangle + \left(C_S^2 \right)^2 \langle M_{ij} M_{ij} \rangle + C_{nl}^2 \langle N_{ij} N_{ij} \rangle$$
$$- 2 \left(C_S^2 \langle L_{ij} M_{ij} \rangle + C_{nl} \langle L_{ij} N_{ij} \rangle - C_S^2 C_{nl} \langle M_{ij} N_{ij} \rangle \right), \tag{22}$$

where $L_{ij}^d = L_{ij} - \tfrac{1}{3}L_{kk}\delta_{ij}$. C_S in the dynamic Smagorinsky model is calculated by minimizing $\mathscr{E}^{\mathrm{Smag}}$ and is

$$C_S^2 = \frac{\langle L_{ij} M_{ij} \rangle}{\langle M_{ij} M_{ij} \rangle}. \tag{23}$$

Likewise, C_S and C_{nl} in the dynamic mixed nonlinear model (Anderson & Meneveau 1999) are obtained from $\partial\mathscr{E}^{\mathrm{mnl}}/\partial C_S^2 = \partial\mathscr{E}^{\mathrm{mnl}}/\partial C_{nl} = 0$ and become

$$C_S^2 = \frac{\langle L_{ij} M_{ij} \rangle \langle N_{ij} N_{ij} \rangle - \langle L_{ij} N_{ij} \rangle \langle M_{ij} N_{ij} \rangle}{\langle M_{ij} M_{ij} \rangle \langle N_{ij} N_{ij} \rangle - \langle M_{ij} N_{ij} \rangle^2}, \tag{24}$$

$$C_{nl} = \frac{\langle L_{ij} N_{ij} \rangle \langle M_{ij} M_{ij} \rangle - \langle L_{ij} M_{ij} \rangle \langle M_{ij} N_{ij} \rangle}{\langle M_{ij} M_{ij} \rangle \langle N_{ij} N_{ij} \rangle - \langle M_{ij} N_{ij} \rangle^2}. \tag{25}$$

Simulations are performed in this paper using these three models (standard Smagorinsky, dynamic Smagorinsky, and dynamic mixed nonlinear model) implemented in a pseudospectral simulation. Two types of filtering are considered: spectral cutoff filtering and Gaussian filtering.

5.2. *Numerical parameters and simulation details*

By invoking the Taylor hypothesis, the spatially decaying grid turbulence of the experiment is analogous to the temporally decaying turbulence. The LES code is pseudospectral, and uses the '3/2 dealiasing rule' and Adams–Bashforth (AB2) temporal integration. The grid size is $N^3 = 128^3$ in physical space. The numerical box size is $L = 5.12$ m, the numerical grid scale, $h = L/N$, is $h = 0.04$ m and the time step is 1.63×10^{-4} s. Simulation parameters are chosen to match those of the experiments as closely as possible. The initial energy distribution is given by the radial three-dimensional energy spectrum deduced from the measurements at $x_1/M = 20$ (see §4.1). In order to start the comparison between experiment and simulation using as realistic initial condition as possible, an initial simulation starting from random-phase Fourier modes is run for sufficiently long time until the derivative skewness becomes steady (we use a time $t = 10M/\langle u_1 \rangle$). The velocity field is then re-scaled in Fourier space so that the energy spectrum corresponds again to the initial energy spectrum of the data at $x_1/M = 20$ (by multiplying the Fourier amplitudes with a coefficient that depends only on wavenumber magnitude).

In the Smagorinsky model C_S is fixed at its classical value for isotropic turbulence in the inertial range (Lilly 1967), $C_S = 0.16$. The model coefficients in the dynamic Smagorinsky and dynamic mixed nonlinear models are calculated using equations (23)–(25) from the resolved velocity fields during the simulation.

Since the simulated turbulence is statistically homogeneous in space, we use volume averaging in determining numerators and denominators in the dynamic model (which minimizes the mean-square error averaged in space, Ghosal *et al.* 1995). As the dynamic coefficients vary quite slowly in time, they are evaluated only every 10 time steps (as in Porté-Agel, Meneveau & Parlange 2000).

The three SGS models (Smagorinsky, dynamic Smagorinsky and dynamic mixed nonlinear models) are considered in conjunction with two different filter types. The first is the spectral cutoff filter. The cutoff filter can be considered as the implicit numerical grid filter when using a pseudospectral code, i.e. in this case $\Delta = h = 0.04$ m. This size corresponds to the case Δ_3 in the experimental data. For the dynamic models a test filter is applied at the larger scale 2Δ. Test filtering should be done using a filter that resembles the implicit grid filter as much as possible in order to preserve scale-similarity. Hence we use a spectral cutoff filter (tests using a Gaussian test filter and a spectral cutoff grid filter–an inconsistent combination–yield poor results, as will be shown with an example).

The second filter type considered is a physical-space, or graded filter (Gaussian or approximated box-filter). As summarized in §1, when comparing LES results with experiments using velocity statistics other than second-order moments, one must use the experimental data that have been filtered with a graded filter before computing the higher-order statistics. Hence, simulations should use an implicit grid filter at scale Δ that corresponds to a graded filter. For instance, this may be accomplished (in an approximate sense) using finite volume or finite difference discretizations. We point out that when using such discretizations the numerical grid spacing h is typically chosen to be smaller than the filter scale Δ in order to account for the spectral leakage of the physical-space filters (see e.g. Shah & Ferziger 1995) where fields
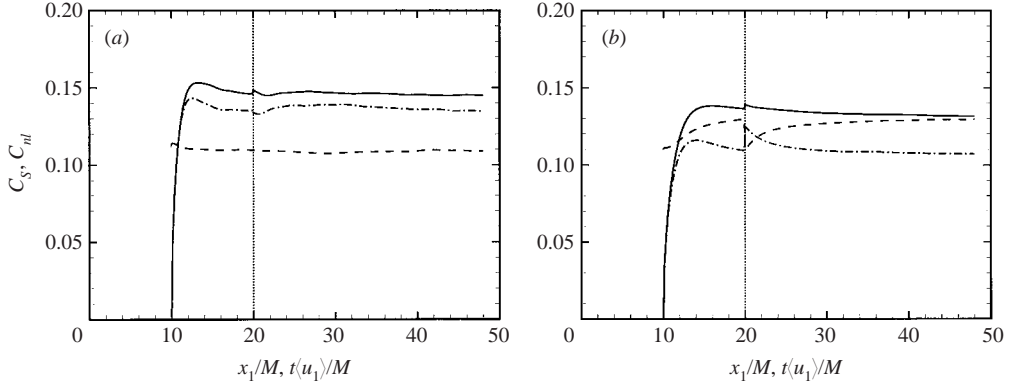
FIGURE 10. Time evolution of dynamic Smagorinsky and nonlinear model coefficients in LES (128^3 simulation) of temporally decaying isotropic turbulence, plotted as a function of $x_1/M = t\langle u_1\rangle/M$: (a) using the spectral cutoff filter with $\Delta = h$ and a cutoff test filter at 2Δ. (b) LES using the graded Gaussian filter with $\Delta = 2h$ and a Gaussian test filter at $2\Delta = 4h$. Solid lines: C_S in the dynamic Smagorinsky model; dash-dot lines: C_S in the dynamic mixed nonlinear model; dashed lines: C_{nl} in the dynamic mixed nonlinear model. In (b) the initial velocity field was Gaussian filtered at $2h$. Vertical dotted line at $x_1/M = 20$ shows the time when the velocity field is re-scaled to conform to the measured experimental spectrum.

require numerical representation at wavenumbers above π/Δ. For consistency and in order to keep the effects of numerical discretization errors to a minimum, we use the same pseudospectral numerical method as used in the context of the spectral cutoff filter. However, to allow approximations of graded filters, we use a numerical mesh spacing that is smaller than the model's filter scale, specifically we use $h = \Delta/2$. The scale Δ enters the simulation through the model expression for the SGS stresses, and is also used to initialize the LES fields at $x_1/M = 20$ (we use a Gaussian filter at scale Δ). For the dynamic models, test filtering is performed at scale $\Delta_T = 2\Delta = 4h$ for determining the model coefficients to be used in the simulation. Again, for consistency and to preserve scale-similarity, we use a Gaussian test filter.

During the time integration no explicit filtering of the simulated velocity fields is performed either to advance the simulation or for post-processing. We take the view that the SGS model should, by itself, cause the simulated fields to develop spectra that are consistent with a field filtered with a graded, physical-space filter at scale $\Delta = 2h$. Since we use the same numerical box size and number of nodes (i.e. $h = 0.04$ m), we now have $\Delta = 0.08$ m, corresponding to the experiments performed with the filter scale Δ_4. The approximated box filter used in the experiment will be considered as an experimental surrogate of a Gaussian filter that is used in the simulations. This approach is justified since the transfer function of the approximated box filter employed in the experiments is quite similar to a Gaussian filter in terms of how it affects the resolved scales in the physical space near the filter size.

5.3. *Results: dynamic model and coefficient evolution*

We begin by documenting briefly the dynamic model performance. The time evolution of the dynamic coefficients is shown in figure 10 as a function of x_1/M (where $x_1 = \langle u_1\rangle t$) for consistency with the subsequent comparisons with the wind tunnel data. The slight discontinuities at $x_1/M = 20$ are due to the re-scaling of the initial velocity field in Fourier space which makes the energy spectrum correspondent again to the initial energy spectrum of the data at $x_1/M = 20$. Comparison with data begins
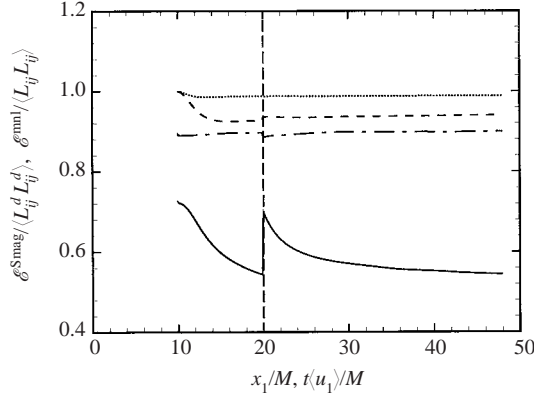
FIGURE 11. Time evolution of normalized dynamic error during simulations. Dotted line: dynamic Smagorinsky model with cutoff filter; dashed line: dynamic Smagorinsky model with Gaussian filter; dash-dot line: dynamic mixed nonlinear model with cutoff filter; solid line: dynamic mixed nonlinear model with Gaussian filter. Vertical dashed line at $x_1/M = 20$ shows the time when velocity field is re-scaled to conform to the measured experimental spectrum.

at $x_1/M = 20$, after which dynamic coefficients remain nearly constant. As expected C_S is about 0.15 for the cutoff grid filter (in figure 10a) and is about 0.13 for the Gaussian filter case (in figure 10b).

In the LES using the dynamic mixed nonlinear model, both the coefficients, C_S and C_{nl}, are also nearly constant as shown in figure 10(a, b), but C_S is lower than that in the dynamic Smagorinsky model. Interestingly, we obtain $C_{nl} \sim 0.13$ in the LES with an initial condition Gaussian-filtered and Gaussian test filter. This value is 30% lower than obtained from *a priori* tests (Liu *et al.* 1999) or simulations using second-order finite difference methods (Anderson & Meneveau 1999), but agrees well with the results from *a priori* tests that focus on eigenvector alignments (Tao *et al.* 2002). Also, it is higher than the value of 1/12 that results from a first-order approximation of the Leonard stress (Leonard 1974) or is often advocated for the dynamic mixed model (Zang, Street & Koseff 1993).

Once the coefficients are determined, the dynamic errors, $\mathscr{E}^{\mathrm{Smag}}$ and $\mathscr{E}^{\mathrm{mnl}}$, in satisfying Germano's identity can be evaluated by equations (21) and (22). Results are shown in figure 11. The dynamic errors are normalized with $\langle L_{ij} L_{ij} \rangle$ or $\langle L_{ij}^d L_{ij}^d \rangle$ corresponding to the errors that result from setting the coefficients to zero (i.e. $\langle L_{ij}^d L_{ij}^d \rangle$ for the dynamic Smagorinsky models shown in equation (21) and $\langle L_{ij} L_{ij} \rangle$ for the dynamic nonlinear models shown in equation (22)). It is clear in figure 11 that the dynamic mixed nonlinear model improves upon the dynamic Smagorinsky model as was reported by Meneveau & Katz (1999) and Anderson & Meneveau (1999). The normalized error in LES performed with a Gaussian-filtered initial condition and a Gaussian test filter is smaller than that obtained when using cutoff grid and test filters.

5.4. *Kinetic energy and energy spectra*

Energy spectra from LES using the Smagorinsky, dynamic Smagorinsky and dynamic mixed nonlinear models are shown in figure 12(a, c, e) (left column). They correspond to the cutoff grid filter at scale h. Energy spectra from LES for the three models for the Gaussian filter are shown in figure 12(b, d, f) (right column). Note that initial spectra at $x_1/M = 20$ agree exactly with the experimental spectrum, by construction
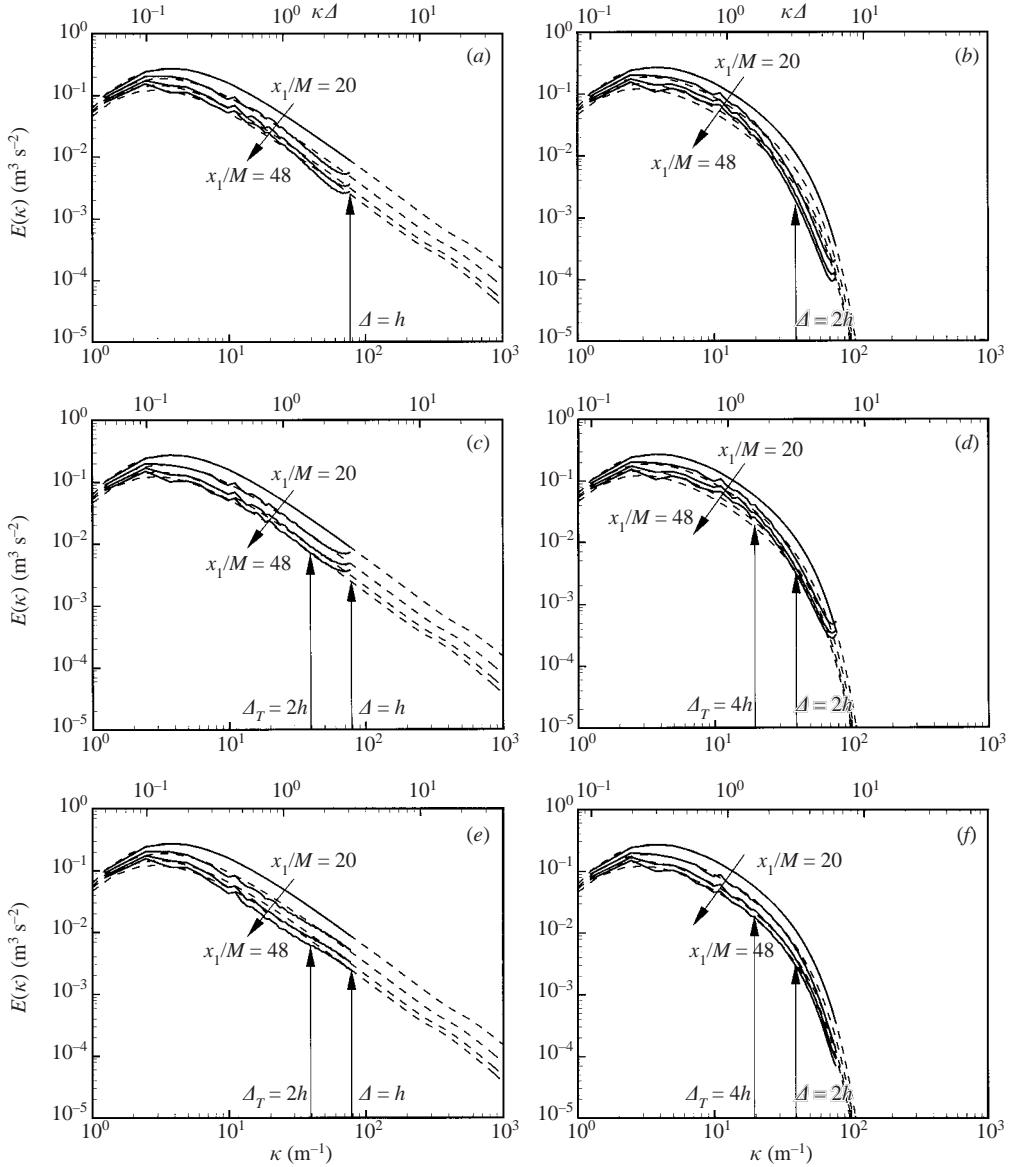
FIGURE 12. Three-dimensional radial energy spectra in decaying isotropic turbulence. The solid and dashed lines represent the results from LES and experiments, respectively. The left column (a, c, e) represents cases with the spectral cutoff filter. The experimental spectra are shown in their entirety without filtering. The filter cutoff is at scale h (i.e. wavenumber $\kappa_{\Delta_3} = \pi/\Delta_3 = 78.5 \, \text{m}^{-1}$ shown by the arrow – test-filter scale is at $\pi/(2\Delta_3)$). The right column (b, d, f) shows cases corresponding to Gaussian filtering at $\Delta_4 = 2h = 0.08 \, \text{m}$. The experimental spectra (dashed lines) are filtered using a radial Gaussian filter. The simulation results (solid lines) are obtained without explicit filtering (except for the initial condition). (a) Non-dynamic Smagorinsky model with a cutoff filter; (b) non-dynamic Smagorinsky model with Gaussian filter; (c) dynamic Smagorinsky model with a cutoff filter; (d) dynamic Smagorinsky model with Gaussian filter; (e) dynamic mixed nonlinear model with a cutoff filter; (f) dynamic mixed nonlinear model with a Gaussian filter.

(cutoff filtered at $\kappa_{\Delta_3} = \pi/\Delta_3$ for the left column and Gaussian-filtered at $\kappa_{\Delta_4} = \pi/\Delta_4$ in the right column). Overall, there is good agreement between the simulations and experiments.

In greater detail, the Smagorinsky model in figure 12(*a*) damps energy at wavenumbers near $\kappa\Delta > 1.2$ and there is a rise near the largest wavenumber (this cusp is well-known and has motivated spectral eddy viscosity models, see Lesieur & Métais 1996). The dynamic Smagorinsky model in figure 12(*c*), by providing a slightly lower coefficient, removes the damping of the energy near $\kappa\Delta \sim 1.6$, but there is still a rise at the cutoff wavenumber. The dynamic mixed nonlinear model with cutoff filtering shown in figure 12(*e*) damps wavenumbers excessively in a range of $0.32 < \kappa\Delta < 1.6$. However it yields accurate spectra near the largest wavenumber, eliminating the rise normally seen with the Smagorinsky model. This is a somewhat unexpected feature of the nonlinear model which in the past has been considered beneficial in terms of stress alignments and correlation coefficients but not in terms of elimination of energy pile-up near the cutoff wavenumber.

The energy spectra for the Gaussian filter cases also show a small rise at the largest wavenumber for the Smagorinsky and dynamic Smagorinsky models and, again, no rise in the energy spectra from the dynamic mixed nonlinear model. The Smagorinsky models (both non-dynamic and dynamic) yield an overprediction of the spectra between $\kappa\Delta = 0.32$ and $\kappa\Delta = 1.6$ and the non-dynamic Smagorinsky model damps too much energy between $\kappa\Delta = 1.6$ and almost up to the grid wavenumber at π/h.

In all the cases considered so far, the test filtering has been applied in a manner that is consistent with the grid-level filter and numerical method. While the discussion above shows that some discrepancies exist for different models and filter types, the overall agreement between measured and simulated spectra appears quite good. However, without presenting extensive results about this issue, we mention that numerous tests with several other, inconsistent, versions of dynamic SGS models yield poor results. As an illustration, consider the case of the dynamic mixed nonlinear model in which the simulation is performed using a spectral cutoff grid filter ($\Delta = h$) but where a Gaussian test filter is used at scale 2Δ. In that case the dynamic model returns coefficients of about $C_S \sim 0.12$ and $C_{nl} \sim 0.12$ and the resulting spectra are shown in figure 13. As opposed to figure 12(*e*) in which the same model is used with a consistent test filter, here the spectra are very poorly predicted, with a severe depletion of energy at intermediate wavenumbers, and a pile-up towards the higher wavenumbers. In this case the model does not provide the correct amount of energy dissipation during the simulation. It can be concluded that the consistent formulation of the dynamic model is crucial.

Next, we turn attention to the decay of total kinetic energy in the resolved scales, as an integral measure of the spectra shown before. The kinetic energy is obtained by integrating the radial spectra shown before according to equations (7) and (8). Figures 14(*a*) and 14(*b*) show the filtered kinetic energy as a function of time or downstream distance. The solid circles represent the filtered kinetic energy from experiments. The cutoff filter cases shown in figure 14(*a*) use a filter scale of $\Delta_3 = 0.04$ m while the Gaussian filter cases in figure 14(*b*) use $\Delta_4 = 0.08$ m. As anticipated from figure 12, the kinetic energy for the cutoff filter cases is well predicted by all models, with a slight underprediction of the kinetic energy by the dynamic mixed model and overprediction by the eddy viscosity models. For the Gaussian filter cases shown in figure 14(*b*), the dynamic mixed model yields better agreement with the spectra. It should be pointed out that if the Smagorinsky model were used with a
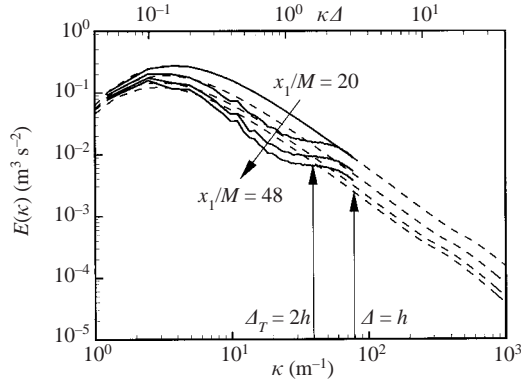
FIGURE 13. Three-dimensional radial energy spectra in LES (128^3 simulation) of decaying isotropic turbulence using dynamic mixed nonlinear model with a cutoff grid filter at h and a Gaussian test filter at $2h$. The solid and dashed lines represent the results from LES and experiments, respectively.
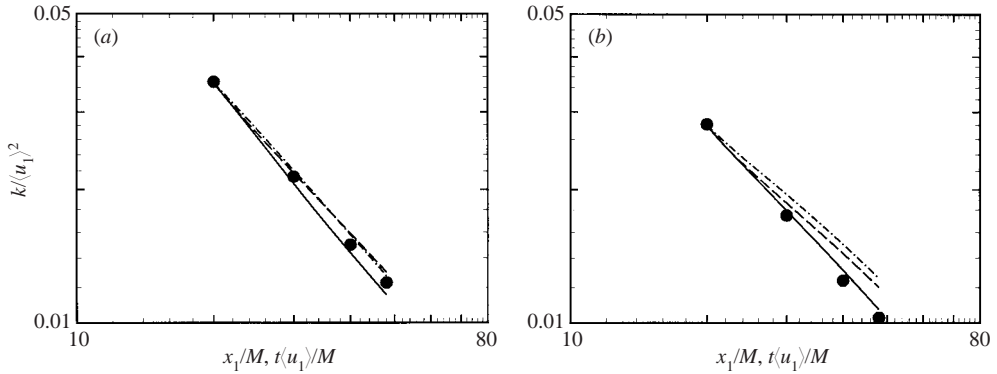
FIGURE 14. Downstream evolution of the kinetic energy of the filtered turbulence: (*a*) spectral cutoff-filtered at $\Delta = h$; (*b*) $\Delta = 2h$ with an initial condition Gaussian filtered at $2h$. The solid circle represents the filtered kinetic energy from experiments. Dashed line: Smagorinsky model; dash-dot line: dynamic Smagorinsky model; solid line: dynamic mixed nonlinear model.

higher value for the coefficient (for Gaussian filters values as high as $C_S = 0.2$ are sometimes used) the agreement could be improved. In the simulations the dynamic model does not yield such high coefficients (even with consistent filtering) and so the decay rate is less. A possible reason is the closeness of the test-filtering scale to the integral scale ($\Delta_T \sim \ell/2$) in this case.

Summarizing the comparisons of kinetic energy and spectra in LES and active-grid turbulence, we find that for the spectral cutoff filter the dynamic Smagorinsky model simulates the energy spectrum more closely at smaller κ, and the dynamic mixed nonlinear model has closer agreement at large κ, while the dynamic mixed nonlinear model yields best results for the Gaussian filter case in which the model filter is set to twice the numerical grid filter.

5.5. *Higher-order statistics of filtered turbulence*

Energy spectra provide complete information about two-point correlations and second-order moments. As already pointed out in §4.2, the statistics of the local

FIGURE 15. Probability density function of the filtered velocity increment $\delta\widetilde{u}_i = \widetilde{u}_i(x_1 + r) - \widetilde{u}_i(x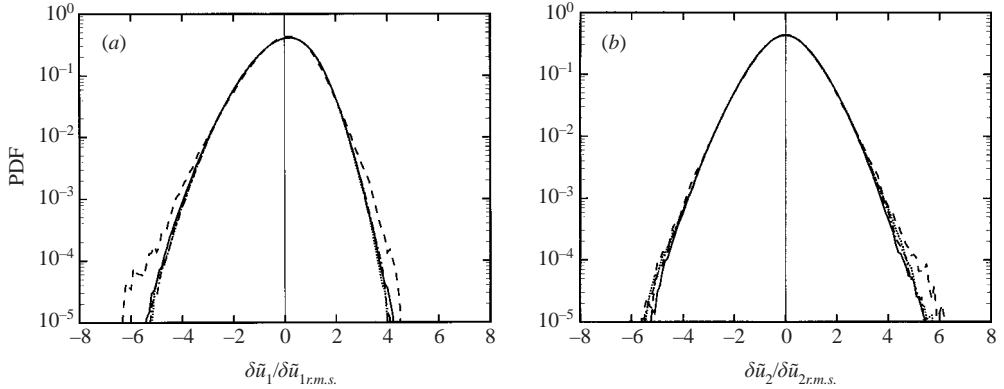_1)$ at $r = \Delta$ and at $x_1/M = 48$. For the data the filter is the graded filter in physical space at $\Delta_4 = 0.08$ m, and the simulation corresponds to the Gaussian filter at $\Delta = 0.08$ m ($\Delta = 2h$). The velocity increments are normalized with their r.m.s. values $\delta\widetilde{u}_{ir.m.s.}$, and $i = 1, 2$: (*a*) $\delta\widetilde{u}_1$ (longitudinal velocity increments); (*b*) $\delta\widetilde{u}_2$ (transverse velocity increments). Dashed line: experimental data; dotted line: Smagorinsky model; dash-dot line: dynamic Smagorinsky model; solid line: dynamic mixed nonlinear model.

turbulence structure can be characterized more fully by studying the filtered velocity increments (see equation (11)). Specifically, we now investigate whether LES provides accurate PDFs of the filtered velocity increments. We limit the comparison to the last time during the decay and compare with the measurements at $x_1/M = 48$. Since the data have been filtered using a graded filter in physical space, we only compare with the simulations using the Gaussian filter. In order to focus attention on the high-order statistics, the measured and simulated velocity increments are normalized with their respective r.m.s. values. These are second-order statistics and as such they have already been taken into account during the comparison of energy spectra in the preceding section.

Figure 15 shows a comparison between PDFs of $\delta\widetilde{u}_i$ from the experiment and LES. The separation distance is equal to the filter scale ($r = \Delta$). For the streamwise velocity component $\delta\widetilde{u}_1$ (figure 15*a*), the distribution is negatively skewed and non-Gaussian behaviour is observed in the tails of the distributions. Interestingly, LES with all three models predict essentially the same PDF behaviour, which is noticeably less intermittent than the measured PDFs. The latter have slightly longer tails.

For the cross-stream velocity component $\delta\widetilde{u}_2$ (figure 15*b*), the distribution is nearly symmetric and smaller differences between the experiment and simulations are observed. However, near the tails of the PDF the dynamic mixed model underestimates slightly the intermittency.

To compare the differences in intermittency more clearly, we measure the hyper-flatness coefficients of various orders. The hyper-flatness factor is defined as

$$F_{\delta\widetilde{u}_i}(n) \equiv \frac{\langle(\delta\widetilde{u}_i)^n\rangle}{(\delta\widetilde{u}_{ir.m.s.})^n}, \qquad (26)$$

where n is an even exponent equal to or greater than 2 (no summation over i). By definition, $F_{\delta\widetilde{u}_i}(2) = 1$. Also, we recall that for a Gaussian random variable of unit variance the hyper-flatness is given by $F_G(n) = (2\pi)^{-1/2} 2^{(n+1)/2} \Gamma[(n+1)/2]$.
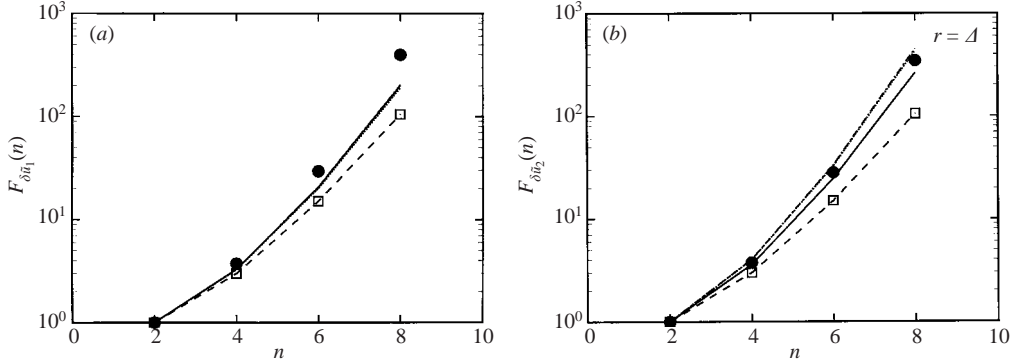
FIGURE 16. Hyper-flatness of the filtered velocity increment $\delta\widetilde{u}_i$, $F_{\delta\widetilde{u}_i}(n) \equiv \langle(\delta\widetilde{u}_i)^n\rangle/(\delta\widetilde{u}_{i\,\mathrm{r.m.s.}})^n$, where n is an even exponent equal to or greater than 2, at $x_1/M = 48$: (a) $\delta\widetilde{u}_1$ at $r = \Delta$; (b) $\delta\widetilde{u}_2$ at $r = \Delta$; Solid circles represent the filtered experimental data. Dotted line: Smagorinsky model; dash-dot line: dynamic Smagorinsky model; solid line: dynamic mixed nonlinear model; dashed line with squares: hyper-flatness of a Gaussian variable.
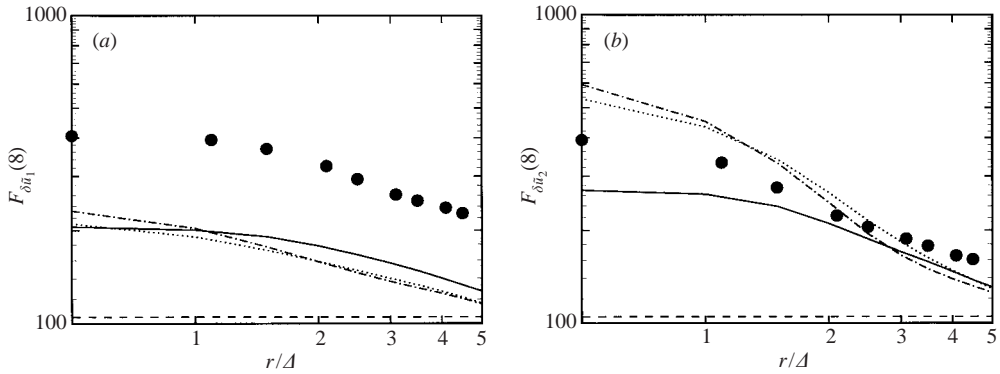
FIGURE 17. Hyper-flatness of the filtered velocity increment $\delta\widetilde{u}_i$, $F_{\delta\widetilde{u}_i}(8) \equiv \langle(\delta\widetilde{u}_i)^8\rangle/(\delta\widetilde{u}_{i\,\mathrm{r.m.s.}})^8$ as a function of displacement, at $x_1/M = 48$: (a) $\delta\widetilde{u}_1$; (b) $\delta\widetilde{u}_2$; solid circles represent the filtered experimental data. Dotted line: Smagorinsky model; dash-dot line: dynamic Smagorinsky model; solid line: dynamic mixed nonlinear model; dashed line: hyper-flatness of Gaussian variable, $F_G(8)$.

Deviations of $F_{\delta\widetilde{u}_i}(n)$ from $F_G(n)$ quantify the deviations from Gaussian behaviour. Figures 16(a) and 16(b) show the hyper-flatness for the streamwise and cross-stream components, $\delta\widetilde{u}_1$ and $\delta\widetilde{u}_2$, respectively, from the filtered experimental data and LES at $x_1/M = 48$ and $r = \Delta$. The filtered experimental data are shown with solid circles. The simulations underestimate the hyper-flatness of the longitudinal velocity component, with the three models giving approximately the same results. Even though the general trends appear to be well predicted, for $n = 8$ the simulations fall only about half-way between the Gaussian and the measured values, i.e. they underestimate longitudinal intermittency quite significantly. As could already be deduced from the PDFs, the situation is different for the transverse velocity increments, where the models differ among themselves but give more realistic results.

Figures 17(a) and 17(b) show similar comparisons for the velocity increments evaluated at several displacements larger than the filter size, for $n = 8$. As r grows

FIGURE 18. Skewness coefficients of the longitudinal structure function as a function of displacement, $x_1/M = 48$: Solid circles: experiment (same as solid line in figure 9); dotted line: Smagorinsky model; dash-dot line: dynamic Smagorinsky model; solid line: dynamic mixed nonlinear model. The vertical arrow corresponds to the integral length scale.
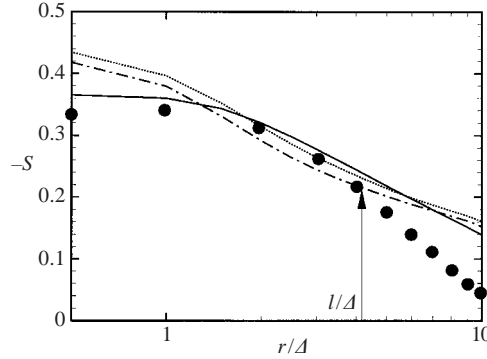
larger and approaches the integral scale ℓ ($\sim 4\Delta$), the statistics approach Gaussian behaviour. Whereas the moments of the longitudinal velocity increments at $r > \Delta$ from the LES show the same trend as discussed above (the simulations underestimate longitudinal intermittency), the moments of the transverse velocity increments at $r > \Delta$ depend on the models. The eddy viscosity models overpredict transverse intermittency at about $r < 3\Delta$ and underpredict it for $r > 3\Delta$. The dynamic mixed nonlinear model underpredicts the transverse intermittency at all $r > \Delta$.

Returning to the case of $r = \Delta$ for longitudinal velocity increments, a possible cause of the higher intermittency in the experimental data compared to simulation could be that the experimental data are only filtered in two directions, whereas the LES fields correspond to three-dimensional filtering. We have examined this possibility by analysing simulation results using two- and three-dimensional filtering at scales four times larger than the grid scale. The PDFs of normalized velocity increments filtered in two or three dimensions are virtually indistinguishable (there is a small difference in the r.m.s. of velocity increments – as expected, the r.m.s. of two-dimensional filtered velocity is slightly larger than that of three-dimensional filtered variables – but the normalized PDFs are insensitive to this difference). We conclude that the measured PDFs accurately represent the PDFs of filtered turbulence and that the effect of two- vs. three-dimensional filtering on the shape of normalized PDFs is negligible.

The other issue concerns convergence of moments. We have checked that all the PDFs multiplied by powers of the velocity increments tend to zero sufficiently fast at the tails for the required moments to converge. Hence the nth-order moments of velocity increments reported in figures 16 and 17 are statistically well converged, up to $n = 8$.

The structure-function skewness of the filtered velocity, defined in equation (12) is evaluated from the simulations and compared to the data. Figure 18 shows the negative of the skewness coefficient as a function of displacement. The experimental data (solid circles) show that $-S$ is about 0.33 at the filter scale $r = \Delta$, and decreases as the separation distance increases. The mixed nonlinear model (solid line) yields a slight overprediction of the skewness at all displacements, but follows the measured trends rather closely, including the curvature. The eddy viscosity models,
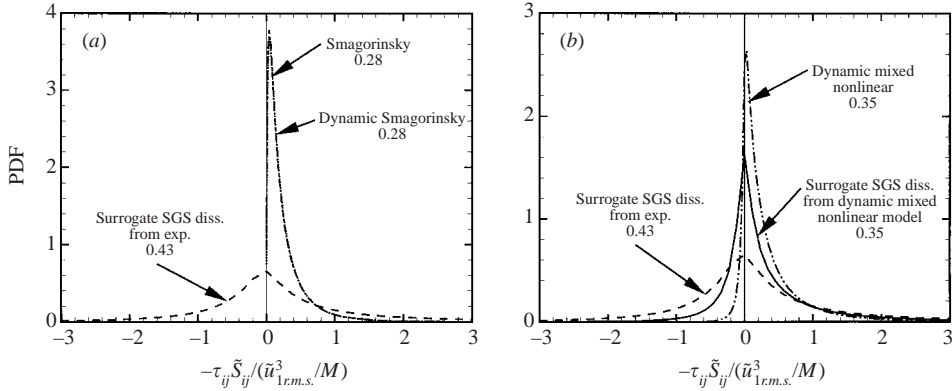
FIGURE 19. PDF of local SGS dissipation, $-\tau_{ij}\widetilde{S}_{ij}$, normalized with $u_{1r.m.s.}^3/M$, at $x_1/M = 48$. The filter type is Gaussian at $\Delta_4 = 2h = 0.08\,\text{m}$: (*a*) eddy viscosity models; (*b*) dynamic mixed nonlinear model. Dashed line: surrogate SGS dissipation from filtered experimental data, $-(\tau_{11}\widetilde{S}_{11} + 2\tau_{22}\widetilde{S}_{22} + 6\tau_{12}\widetilde{S}_{12})$; dotted line: $-\tau_{ij}\widetilde{S}_{ij}$ from Smagorinsky model; dash-dot line: $-\tau_{ij}\widetilde{S}_{ij}$ from dynamic Smagorinsky model; dashed-dot-dot line: $-\tau_{ij}\widetilde{S}_{ij}$ from dynamic mixed nonlinear model; solid line: Surrogate SGS dissipation from dynamic mixed nonlinear model, $-(\tau_{11}\widetilde{S}_{11} + 2\tau_{22}\widetilde{S}_{22} + 6\tau_{12}\widetilde{S}_{12})$. The numbers represent the mean SGS dissipations.

while reproducing the general order of magnitude of the skewness, yield a qualitatively different curvature of $S(r)$, and overpredict the skewness at $r \to 0$.

5.6. *SGS dissipation and stress*

In this section we compare variables that are defined in terms of the SGS velocity field, as measured in the experiments and predicted by the SGS models during the simulations. A variable of interest is the local SGS energy dissipation, defined as $-\tau_{ij}\widetilde{S}_{ij}$. Its average value enters as a sink term in the mean kinetic energy budget of the resolved velocity field. The local dissipation has generated much interest because it indicates the presence of 'backscatter' of energy from small to large scales, when $-\tau_{ij}\widetilde{S}_{ij} < 0$ (Piomelli *et al.* 1991).

Figure 19 shows the PDF of the local SGS dissipation computed at $x_1/M = 48$ for the graded, physical-space filter at $\Delta_4 = 2h$. The dashed line represents the experimental values obtained from the filtered experimental data. Since we do not measure all of the terms comprising the tensor contraction of $-\tau_{ij}\widetilde{S}_{ij}$, as in Liu *et al.* (1994) we compute an experimental surrogate SGS dissipation $-(\tau_{11}\widetilde{S}_{11} + 2\tau_{22}\widetilde{S}_{22} + 6\tau_{12}\widetilde{S}_{12})$. The data are normalized with $u_{1r.m.s.}^3/M$. We observe a significant fraction of the data where the local SGS dissipation is negative, which indicates the backscatter of energy. The numbers shown in the figures represent the mean SGS dissipations, also normalized with $u_{1r.m.s.}^3/M$. Under conditions of quasi-equilibrium, the mean value should equal the molecular dissipation ϵ. The measured average value is $0.43 \times u_{1r.m.s.}^3/M = 3.55\,\text{m}^2\,\text{s}^{-3}$, i.e. about 4% larger than ϵ measured at $x_1/M = 48$ (see table 1).

We now examine the PDFs of modelled local SGS dissipation from the LES, also at $x_1/M = 48$. As shown in figure 19(*a*), by definition the Smagorinsky and dynamic Smagorinsky models give only positive dissipation. As shown in figure 19(*b*), the mixed nonlinear model allows backscatter of energy. The PDF of the surrogate SGS dissipation, $-(\tau_{11}\widetilde{S}_{11} + 2\tau_{22}\widetilde{S}_{22} + 6\tau_{12}\widetilde{S}_{12})$, from the dynamic mixed nonlinear model
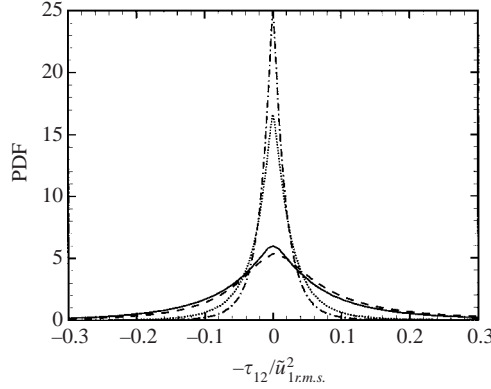
FIGURE 20. PDF of SGS shear stress, τ_{12}, normalized with $u^2_{1\text{r.m.s.}}$ at $x_1/M = 48$. The filter type is Gaussian at $\Delta_4 = 2h = 0.08$ m. Dashed line: experiment; dotted line: Smagorinsky model; dash-dot line: dynamic Smagorinsky model; solid line: dynamic mixed nonlinear model.

is also plotted in figure 19(*b*) for a comparison with that from the experiment. The numbers shown in the figures representing the normalized mean SGS dissipations show that the eddy viscosity models underpredict the SGS dissipation by about 35%, while the dynamic mixed model underpredicts the real measured SGS dissipation by about 19%. Self-consistently, the underprediction of dissipation of the models is consistent with the slower decay of kinetic energy in the simulations as observed in figure 14(*b*). While the mean SGS dissipations of the simulations and experiment are of similar order of magnitude, the PDFs of local SGS dissipation from the simulations are quite different from that of the experimental SGS dissipation.

Another SGS variable which is of direct interest in LES is the SGS stress tensor. A comparison of the PDF of SGS shear stress, τ_{12}, from the experiment, Smagorinsky, dynamic Smagorinsky and dynamic mixed nonlinear models at $x_1/M = 48$ is shown in figure 20. In isotropic turbulence the mean shear (off-diagonal) stress vanishes, consistent with the symmetric shape of the PDFs shown. The Smagorinsky and dynamic Smagorinsky models give narrow distributions, severely underpredicting the r.m.s. and magnitudes of the local stresses. Interestingly, the dynamic mixed nonlinear model predicts the r.m.s. and PDF of the SGS shear stress quite accurately.

6. Summary and conclusions

Experimental measurements performed in the Corrsin wind tunnel have been used to generate a database of decaying isotropic turbulence. The main objectives of this study are to update the results of Comte-Bellot & Corrsin (1971) based on turbulence at high Reynolds number, and to provide more data and details of interest in studies of LES. High-Reynolds-number conditions ($Re_\lambda \approx 720$) are achieved using an active grid system. Careful analysis of spectra shows that the anisotropy of the turbulence (15%) with the present configuration is limited to the largest scales of the flow, of the order of the wind tunnel height and that the inertial-range dynamics is very nearly isotropic. The large-scale anisotropy is acceptable for the purpose of generating a database for LES, since at those large scales the experimental conditions differ from numerical simulations using periodic boundary conditions in a box anyway.

The radial three-dimensional energy spectra at all the measurement locations are deduced from the measured longitudinal one-dimensional energy spectra. They all have a clear inertial range with a slope of $-5/3$ over 1.5 decades of wavenumber. To allow for smooth transformations between one-dimensional and radial spectra, as well as to simplify comparisons with simulations, the three-dimensional energy spectra are presented using an explicit form that reproduces in detail the measured behaviours. The velocity spectra provide full account of the two-point, second-order moments during the decay. For the purpose of documenting higher-order statistics of the turbulence structure at scales that are comparable to those resolved during LES, a probe array composed of four X-wire sensors is used and two-dimensional box filtering in the streamwise and cross-stream directions is applied to the experimental data. We document PDFs of longitudinal and transverse filtered velocity increments at various filtering scales and measure the hyper-flatness and skewness coefficients of velocity increments. These data are presented in more detail in tabular form in the Appendix.

Large-eddy simulations of decaying isotropic turbulence are performed using three different SGS models: the Smagorinsky, dynamic Smagorinsky and dynamic mixed nonlinear models. The simulation results are compared directly to the experimental data in order to investigate the effects of different SGS models on the resolved velocity statistics, and also on some statistics of the modelled SGS fields. Overall, the various LES models predict fairly accurate second-order statistics (spectra), when models are formulated consistently (i.e. dynamic models using the same filter type as the implicit grid filter). For the spectral cutoff filter, the dynamic Smagorinsky model simulates the energy spectrum more closely at smaller κ, and the dynamic mixed nonlinear model has closer aggrement at large κ, while for the graded physical-space filters it is the dynamic mixed nonlinear model that provides the best agreement with the measured spectra. These findings are consistent with the early work presented in Piomelli *et al.* (1988) who argued that the Smagorinsky model was consistent with a cutoff filter whereas the mixed model was more justified in the context of graded physical-space filters. Present results show that these arguments hold also when using dynamic versions of these models.

Comparison of higher-order statistics from LES and experiments, such as PDFs of filtered velocity increments, are performed in the context of graded filters only (since the experimental data could not be filtered in the lateral direction using spectral cutoff filters). The simulations are performed using a numerical discretization that is finer than the filter scale, and are initialized using Gaussian-filtered experimental energy spectra at the initial time. LES using any of the three models considered underpredicts the intermittency level of the longitudinal velocity increment. The tails in PDFs are less extended, and the hyper-flatness coefficients fall midway between the data and Gaussian values. Such deviations are significant, but they occur at displacements of the order of the filter scale. The LES results using eddy-viscosity SGS models are slightly more intermittent than the measured transverse velocity increments. Conversely, the dynamic mixed nonlinear model slightly underpredicts the intermittency of transverse velocity increments. The latter model predicts more realistic trends for the third-order structure function (skewness).

Comparisons of measured surrogate SGS dissipation $-\tau_{ij}\widetilde{S}_{ij}$ with the SGS dissipation predicted by the models show significant differences in their PDFs. As is well-known the eddy viscosity models do not predict backscatter, but the dynamic mixed nonlinear model also does not provide as much backscatter as shown in measurements. More research is needed to examine whether this difference is related to

the SGS models' deficiency in reproducing high enough intermittency of longitudinal velocity increments. The mixed nonlinear model, on the other hand, provides good predictions of SGS shear stress variance and its PDF, whereas the SGS stress variance is severely underpredicted by the eddy viscosity models.

Overall, the present results confirm the generally held view that LES can provide good statistics of resolved velocity in isotropic turbulence, where the most important role of SGS models is to provide the correct rate of mean energy dissipation. The numerical results of Langford & Moser (1999) based on their 'optimal LES model' (which is based on two-point information and is therefore more sophisticated than the simple local models considered here) also showed that statistics of resolved turbulence in LES are well predicted if the dissipation rate in Fourier space is properly reproduced. However, by using detailed comparisons under carefully controlled conditions, the present work has identified some differences between LES and experimental data in high-order statistics and tails of the velocity increment PDFs at scales comparable to the filter scales.

It would be interesting to explore whether these differences can be reduced using 'optimal' models as described in Langford & Moser (1999) or using other modelling approaches. We recall that a number of new SGS models have been proposed in recent years, such as the vortex method of Pullin & Saffman (1993) and Misra & Pullin (1997), the fractal model of Scotti & Meneveau (1999), the filtered structure function model in Lesieur & Métais (1996), the deconvolution models of Stolz, Adams & Kleiser (2001) and several others. The present study provides detailed experimental data against which such new SGS modelling concepts can be tested in considerable detail and at a high Reynolds number.

Appendix. Measured data in tabular form

The main experimental results of the present study are documented in this Appendix in tabular form. Table 2 shows the measured one-dimensional spectra, $E_{11}(\kappa)$ and $E_{22}(\kappa)$, in a range of wavenumbers from $\kappa_1 = 1\,\mathrm{m}^{-1}$ to $4000\,\mathrm{m}^{-1}$ in 21 logarithmically spaced wavenumber bands. Table 3 presents the PDF value of longitudinal and transverse velocity increments at a single filter scale (Δ_4) and two displacement values. Table 4 shows the measured skewness and hyper-flatness factors for filtered velocity increments at two displacements.

The radial energy spectra fitted from the data at all four downstream distances can be represented by

$$E(\kappa) = 1.613\ \epsilon^{2/3}\kappa^{-5/3}\left[\frac{\kappa\ell}{[(\kappa\ell)^{1.2}+0.39]^{0.833}}\right]^{5/3+4}\mathrm{e}^{-2.1\ \kappa\eta}$$

$$\times\left[1\ +\ 0.522\ \left(\frac{1}{\pi}\arctan\{10\ \log_{10}(\kappa\eta)+12.58\}+\tfrac{1}{2}\right)\right],\quad (A\,1)$$

where ϵ, ℓ and η are parameters that depend upon x_1/M and that are tabulated in table 1.

$\kappa_{1,m}$ (m^{-1})	$\kappa_{1,m+1}$ (m^{-1})	$\overline{E}_{11}(\kappa_1, x_1)$ (m^{3}s^{-2})				$\overline{E}_{22}(\kappa_1, x_1)$ (m^{3}s^{-2})			
		$x_1/M{=}20$	$x_1/M{=}30$	$x_1/M{=}40$	$x_1/M{=}48$	$x_1/M{=}20$	$x_1/M{=}30$	$x_1/M{=}40$	$x_1/M{=}48$
1.00	1.48	4.48×10^{-1}	2.89×10^{-1}	2.14×10^{-1}	1.75×10^{-1}	8.18×10^{-2}	5.15×10^{-2}	3.93×10^{-2}	3.30×10^{-2}
1.48	2.20	3.47×10^{-1}	2.46×10^{-1}	1.79×10^{-1}	1.54×10^{-1}	1.05×10^{-1}	6.75×10^{-2}	5.09×10^{-2}	4.17×10^{-2}
2.20	3.27	2.91×10^{-1}	2.23×10^{-1}	1.46×10^{-1}	1.29×10^{-1}	1.37×10^{-1}	9.32×10^{-2}	6.95×10^{-2}	5.58×10^{-2}
3.27	4.85	2.30×10^{-1}	1.46×10^{-1}	1.01×10^{-1}	8.85×10^{-2}	1.37×10^{-1}	8.79×10^{-2}	6.22×10^{-2}	5.20×10^{-2}
4.85	7.20	1.82×10^{-1}	9.81×10^{-2}	6.95×10^{-2}	5.75×10^{-2}	1.61×10^{-1}	8.91×10^{-2}	5.89×10^{-2}	4.64×10^{-2}
7.20	10.69	9.75×10^{-2}	5.43×10^{-2}	3.65×10^{-2}	2.98×10^{-2}	9.69×10^{-2}	5.60×10^{-2}	3.75×10^{-2}	3.13×10^{-2}
10.69	15.87	5.16×10^{-2}	2.84×10^{-2}	1.94×10^{-2}	1.54×10^{-2}	5.86×10^{-2}	3.36×10^{-2}	2.31×10^{-2}	1.86×10^{-2}
15.87	23.56	2.82×10^{-2}	1.56×10^{-2}	1.04×10^{-2}	8.48×10^{-3}	3.29×10^{-2}	1.87×10^{-2}	1.32×10^{-2}	1.06×10^{-2}
23.56	34.97	1.50×10^{-2}	8.19×10^{-3}	5.50×10^{-3}	4.42×10^{-3}	1.83×10^{-2}	1.04×10^{-2}	7.17×10^{-3}	5.68×10^{-3}
34.97	51.91	7.85×10^{-3}	4.30×10^{-3}	2.84×10^{-3}	2.27×10^{-3}	9.79×10^{-3}	5.49×10^{-3}	3.81×10^{-3}	3.02×10^{-3}
51.91	77.05	4.11×10^{-3}	2.23×10^{-3}	1.46×10^{-3}	1.16×10^{-3}	5.11×10^{-3}	2.90×10^{-3}	1.96×10^{-3}	1.57×10^{-3}
77.05	114.37	2.12×10^{-3}	1.16×10^{-3}	7.68×10^{-4}	6.17×10^{-4}	2.67×10^{-3}	1.48×10^{-3}	1.01×10^{-3}	8.06×10^{-4}
114.37	169.76	1.12×10^{-3}	6.13×10^{-4}	4.13×10^{-4}	3.27×10^{-4}	1.38×10^{-3}	7.76×10^{-4}	5.27×10^{-4}	4.19×10^{-4}
169.76	251.98	5.89×10^{-4}	3.28×10^{-4}	2.21×10^{-4}	1.77×10^{-4}	7.23×10^{-4}	4.09×10^{-4}	2.84×10^{-4}	2.26×10^{-4}
251.98	374.02	3.16×10^{-4}	1.74×10^{-4}	1.16×10^{-4}	9.16×10^{-5}	3.88×10^{-4}	2.24×10^{-4}	1.56×10^{-4}	1.25×10^{-4}
374.02	555.17	1.65×10^{-4}	8.80×10^{-5}	5.73×10^{-5}	4.44×10^{-5}	2.13×10^{-4}	1.22×10^{-4}	8.43×10^{-5}	6.72×10^{-5}
555.17	824.05	8.05×10^{-5}	4.11×10^{-5}	2.55×10^{-5}	1.91×10^{-5}	1.13×10^{-4}	6.30×10^{-5}	4.20×10^{-5}	3.27×10^{-5}
824.05	1223.15	3.53×10^{-5}	1.66×10^{-5}	9.67×10^{-6}	6.97×10^{-6}	5.50×10^{-5}	2.87×10^{-5}	1.81×10^{-5}	1.36×10^{-5}
1223.15	1815.54	1.31×10^{-5}	5.57×10^{-6}	2.96×10^{-6}	2.03×10^{-6}	2.28×10^{-5}	1.09×10^{-5}	6.28×10^{-6}	4.51×10^{-6}
1815.54	2694.84	3.96×10^{-6}	1.50×10^{-6}	7.21×10^{-7}	4.67×10^{-7}	7.58×10^{-6}	3.21×10^{-6}	1.68×10^{-6}	1.14×10^{-6}
2694.84	4000.00	1.01×10^{-6}	3.50×10^{-7}	1.69×10^{-7}	1.03×10^{-7}	1.89×10^{-6}	6.93×10^{-7}	3.26×10^{-7}	2.08×10^{-7}

TABLE 2. Measured longitudinal energy spectra, $\overline{E}_{11}$ and $\overline{E}_{22}$ at $x_1/M = 20$, 30, 40 and 48. $\overline{E}_{11}$ and $\overline{E}_{22}$ are calculated by $(\kappa_{m+1} - \kappa_m)^{-1} \int_{\kappa_m}^{\kappa_{m+1}} E_{11} d\kappa_1$ and $(\kappa_{m+1} - \kappa_m)^{-1} \int_{\kappa_m}^{\kappa_{m+1}} E_{22} d\kappa_1$. (The tabulated values differ from those in the print version of this article: The table as published in the JFM article erroneously displays the energy integrated in wavenumber bins, but without normalizing with the width of the bins. The table above is the same data but now properly normalized, and corresponds to the spectra shown in Figure 4.)

$\delta\tilde{u}_i/\delta\tilde{u}_{i\mathrm{r.m.s.}}$	PDF ($\delta\tilde{u}_1/\delta\tilde{u}_{1\mathrm{r.m.s.}}$)		PDF ($\delta\tilde{u}_2/\delta\tilde{u}_{2\mathrm{r.m.s.}}$)	
	$r = \Delta_4$	$r = 2\Delta_4$	$r = \Delta_4$	$r = 2\Delta_4$
−6.5	0.250×10^{-5}	0.806×10^{-5}	–	–
−6.0	0.350×10^{-4}	0.364×10^{-4}	–	–
−5.5	0.553×10^{-4}	0.339×10^{-4}	0.170×10^{-4}	–
−5.0	0.140×10^{-3}	0.107×10^{-3}	0.925×10^{-4}	0.145×10^{-4}
−4.5	0.502×10^{-3}	0.441×10^{-3}	0.219×10^{-3}	0.130×10^{-3}
−4.0	0.156×10^{-2}	0.106×10^{-2}	0.748×10^{-3}	0.453×10^{-3}
−3.5	0.394×10^{-2}	0.384×10^{-2}	0.263×10^{-2}	0.182×10^{-2}
−3.0	0.104×10^{-1}	0.962×10^{-2}	0.715×10^{-2}	0.599×10^{-2}
−2.5	0.239×10^{-1}	0.248×10^{-1}	0.193×10^{-1}	0.194×10^{-1}
−2.0	0.526×10^{-1}	0.551×10^{-1}	0.497×10^{-1}	0.510×10^{-1}
−1.5	0.111	0.114	0.112	0.117
−1.0	0.207	0.215	0.223	0.228
−0.5	0.332	0.332	0.364	0.368
−0.0	0.426	0.420	0.442	0.427
0.5	0.394	0.393	0.367	0.362
1.0	0.259	0.260	0.223	0.228
1.5	0.116	0.120	0.112	0.116
2.0	0.409×10^{-1}	0.406×10^{-1}	0.479×10^{-1}	0.506×10^{-1}
2.5	0.131×10^{-1}	0.133×10^{-1}	0.194×10^{-1}	0.182×10^{-1}
3.0	0.374×10^{-2}	0.349×10^{-2}	0.734×10^{-2}	0.649×10^{-2}
3.5	0.893×10^{-3}	0.740×10^{-3}	0.277×10^{-2}	0.196×10^{-2}
4.0	0.134×10^{-3}	0.185×10^{-3}	0.753×10^{-3}	0.614×10^{-3}
4.5	0.167×10^{-4}	0.584×10^{-5}	0.279×10^{-3}	0.193×10^{-3}
5.0	–	–	0.121×10^{-3}	0.478×10^{-4}
5.5	–	–	0.867×10^{-4}	0.275×10^{-4}
6.0	–	–	0.139×10^{-4}	–

TABLE 3. PDFs of filtered velocity increments at $x_1/M = 48$ at $r = \Delta_4$ and $r = 2\Delta_4$. Missing values are not sufficiently converged.

	$-S$	$F_{\delta\tilde{u}_1}(4)$	$F_{\delta\tilde{u}_1}(6)$	$F_{\delta\tilde{u}_1}(8)$	$F_{\delta\tilde{u}_1}(10)$	$F_{\delta\tilde{u}_2}(4)$	$F_{\delta\tilde{u}_2}(6)$	$F_{\delta\tilde{u}_2}(8)$	$F_{\delta\tilde{u}_2}(10)$
$r = \Delta_4$	0.340	3.75	29.5	399	8051	3.76	28.2	346	6139
$r = 2\Delta_4$	0.312	3.60	26.4	331	6390	3.49	22.8	229	3169

TABLE 4. Skewnesses and hyper-flatnesses of filtered velocity increments at $x_1/M = 48$ at $r = \Delta_4$ and $r = 2\Delta_4$.

REFERENCES

ACKERMANN, C. & MÉTAIS, O. 2001 A modified selective structure function subgrid-scale model. *J. Turbulence* **2**, 1–27.

ANDERSON, R. & MENEVEAU, C. 1999 Effects of the similarity model in finite-difference LES of isotropic turbulence using a Lagrangian dynamic mixed model. *Flow Turbul. Combust.* **62**, 201–225.

BATCHELOR, G. K. 1953 *The Theory of Homogeneous Turbulence*. Cambridge University Press.

BORUE, V. & ORSZAG, S. 1998 Local energy flux and subgrid-scale statistics in three-dimensional turbulence. *J. Fluid Mech.* **366**, 1–31.

CERUTTI, S. & MENEVEAU, C. 2000 Statistics of filtered velocity in grid and wake turbulence. *Phys. Fluids* **12**, 1143–1165.

CERUTTI, S., MENEVEAU, C. & KNIO, O. M. 2000 Spectral and hyper eddy viscosity in high-Reynolds-number turbulence. *J. Fluid Mech.* **421**, 307–338.

CLARK, R. A., FERZIGER, J. H. & REYNOLDS, W. C. 1979 Evaluation of subgrid-scale models using an accurately simulated turbulent flow. *J. Fluid Mech.* **91**, 1–16.

COMTE-BELLOT, G. & CORRSIN, S. 1966 The use of a contraction to improve the isotropy of grid-generated turbulence. *J. Fluid Mech.* **25**, 657–682.

COMTE-BELLOT, G. & CORRSIN, S. 1971 Simple Eulerian time correlation of full- and narrow-band velocity signals in grid-generated, 'isotropic' turbulence. *J. Fluid Mech.* **48**, 273–337 (referred to herein as CBC).

DANTINNE, G., JEANMART, H., WINCKELMANS, G. S., LEGAT, V. & CARATI, D. 1998 Hyperviscosity and vorticity-based models for subgrid scale modeling. *Appl. Sci. Res.* **59**, 409–420.

GAD-EL-HAK, M. & CORRSIN, S. 1974 Measurements of the nearly isotropic turbulence behind a uniform jet grid. *J. Fluid Mech.* **62**, 115–143.

GERMANO, M., PIOMELLI, U., MOIN, P. & CABOT, W. H. 1991 A dynamic subgrid-scale eddy viscosity model. *Phys. Fluids* A **3**, 1760–1765.

GHOSAL, S., LUND, T. S., MOIN, P. & AKSELVOLL, K. 1995 A dynamic localization model for large-eddy simulation of turbulent flows. *J. Fluid Mech.* **286**, 229–255.

KANG, H. S. & MENEVEAU, C. 2001 Passive scalar anisotropy in a heated turbulent wake: new observations and implications for large-eddy simulations. *J. Fluid Mech.* **442**, 161–170.

LANGFORD, J. A. & MOSER, R. D. 1999 Optimal LES formulations for isotropic turbulence. *J. Fluid Mech.* **398**, 321–346.

LARSSEN, J. V. & DEVENPORT, W. J. 2002 The generation of high Reynolds number homogeneous turbulence. *Am. Inst. Aeronaut. Astronaut. Paper* 2002-2861.

LEONARD, A. 1974 Energy cascade in large-eddy simulations of turbulent fluid flows. *Adv. Geophys.* **18**, 237–248.

LEONARD, A. 1997 Large-eddy simulation of chaotic convection and beyond. *Am. Inst. Aeronaut. Astronaut. Paper* 97-0204, pp. 1–8.

LESIEUR, M. & MÉTAIS, O. 1996 New trends in large-eddy simulations of turbulence. *Annu. Rev. Fluid Mech.* **28**, 45–82.

LILLY, D. K. 1967 The representation of small-scale turbulence in numerical simulation experiments. *Proc. IBM Scientific Computing Symposium on Environmental Sciences* (ed. H. H. Goldstein), pp. 195–210. IBM form no. 320-1951.

LINDBORG, E. 1999 Correction to the four-fifths law due to variations of the dissipation. *Phys. Fluids* **11**, 510–512.

LIU, S., MENEVEAU, C. & KATZ, J. 1994 On the properties of similarity subgrid-scale models as deduced from measurements in a turbulent jet. *J. Fluid Mech.* **275**, 83–119.

LUNDGREN, T. S. 2002 Kolmogorov two-thirds law by matched asymptotic expansion. *Phys. Fluids* **14**, 638–642.

MAKITA, H. 1991 Realization of a large-scale turbulence field in a small wind tunnel. *Fluid Dyn. Res.* **8**, 53–64.

MENEVEAU, C. 1994 Statistics of turbulence subgrid-scale stresses: Necessary conditions and experimental tests. *Phys. Fluids* **6**, 815–833.

MENEVEAU, C. & KATZ, J. 1999 Dynamic testing of subgrid models in large eddy simulation based on the Germano identity. *Phys. Fluids* **11**, 245–247.

MENEVEAU, C. & KATZ, J. 2000 Scale-invariance and turbulence models for large-eddy simulation. *Annu. Rev. Fluid Mech.* **32**, 1–32.

MENEVEAU, C., LUND, T. S. & CABOT, W. H. 1996 A Lagrangian dynamic subgrid-scale model of turbulence. *J. Fluid Mech.* **319**, 353–385.

MISRA, A. & PULLIN, D. I. 1997 A vortex-based subgrid stress model for large-eddy simulation. *Phys. Fluids* **9**, 2443–2454.

MOIN, P., SQUIRES, K., CABOT, W. & LEE, S. 1991 A dynamic subgrid-scale model for compressible turbulence and scalar transport. *Phys. Fluids* A **3**, 2746–2757.

MYDLARSKI, L. & WARHAFT, Z. 1996 On the onset of high-Reynolds-number grid-generated wind tunnel turbulence. *J. Fluid Mech.* **320**, 331–368.

MYDLARSKI, L. & WARHAFT, Z. 1998 Passive scalar statistics in high-Péclet-number grid turbulence. *J. Fluid Mech.* **358**, 135–175.

O'NEIL, J. & MENEVEAU, C. 1997 Subgrid-scale stresses and their modelling in a turbulent plane wake. *J. Fluid Mech.* **349**, 253–293.

PIOMELLI, U. 1999 Large-eddy simulation: achievements and challenges. *Prog. Aerospace Sci.* **35**, 335–362.

PIOMELLI, U., CABOT, W. H., MOIN, P. & LEE, S. S. 1991 Subgrid-scale backscatter in turbulent and transitional flows. *Phys. Fluids* A **3**, 1766–1771.

POORTE, R. E. G. 1998 On the motion of bubbles in active grid generated turbulent flows. PhD thesis, University of Twente.

POPE, S. B. 2000 *Turbulent Flows*. Cambridge University Press.

PORTÉ-AGEL, F., MENEVEAU, C. & PARLANGE, M. B. 2000 A scale-dependent dynamic model for large-eddy simulation: application to a neutral atmospheric boundary layer. *J. Fluid Mech.* **415**, 261–284.

PULLIN, D. I. & SAFFMAN, P. G. 1993 On the Lundgren–Townsend model of turbulent fine scales. *Phys. Fluids* A **5**, 126–145.

SCOTTI, A. & MENEVEAU, C. 1999 A fractal model for large eddy simulation of turbulent flow. *Physica* D **127**, 198–232.

SHAH, J. & FERZIGER, J. H. 1995 A new non-eddy viscosity subgrid-scale model and its application to channel flow. *Center for Turbulence Research Ann. Res. Briefs, Stanford University*, pp. 73–90.

SMAGORINSKY, J. 1963 General circulation experiments with the primitive equations. I. The basic experiment. *Mon. Weather Rev.* **91**, 99–164.

SREENIVASAN, K. R. 1995 On the universality of the Kolmogorov constant. *Phys. Fluids* **7**, 2778–2784.

STOLZ, S., ADAMS, N. A. & KLEISER, L. 2001 The approximate deconvolution model for large-eddy simulations of compressible flows and its application to shock-turbulent-boundary-layer interaction. *Phys. Fluids* **13**, 2985–3001.

TAO, B., KATZ, J. & MENEVEAU, C. 2002 Statistical geometry of subgrid-scale stresses determined from holographic particle image velocimetry measurements. *J. Fluid Mech.* **457**, 35–78.

ZANG, Y., STREET, R. L. & KOSEFF, J. 1993 A dynamic mixed subgrid-scale model and its application to turbulent recirculating flows. *Phys. Fluids* A **5**, 3186–3196.